CCI

BIOMASS

Phase IV

CLIMATE ASSESSMENT REPORT

YEAR 7

VERSION 7.0

DOCUMENT REF:	CCI_BIOMASSAGB_CAR_V7
DELIVERABLE REF:	D5.1_CAR
VERSION:	7.0
CREATION DATE:	2026-04-01
LAST MODIFIED	

Document Authorship

	NAME	FUNCTION	ORGANISATION	SIGNATURE	DATE
PREPARED	P. Ciais	WP5000 Lead	LSCE		
PREPARED	Y. Xu	WP5000 Researcher	LSCE		
PREPARED	Y. Hui	WP5000 Researcher	Peking University		
PREPARED	M. Santoro	Project Researcher	Gamma		
VERIFIED	R. Lucas	Project Manager	Aberystwyth University		
VERIFIED	S. Quegan	Science Leader	Sheffield University		
VERIFIED	A. Harris	Project Coordinator	Aberystwyth University		

Document Distribution

ORGANISATION	NAME	QUANTITY
ESA	Clement Mathieu Jacques Albergel	

Document History

VERSION	DATE	DESCRIPTION	APPROVED
7.0	2026-04-01	First draft version	
7.0	2026-05-25	Finalised version	

Document Change Record (from Year 1 to Year 2)

VERSION	DATE	DESCRIPTION	APPROVED

TABLE OF CONTENTS

LIST OF FIGURES *4*

LIST OF TABLES *6*

SYMBOLS AND ACRONYMS *7*

1 Summary *8*

2 Evaluation of vegetation above-ground biomass carbon from CMIP6 ESMs using global satellite-based estimates *9*

2.1.1 ESA CCI Biomass dataset 10

2.1.2 CMIP6 ESM simulations 10

2.1.3 Auxiliary datasets 11

2.1.4 Statistical analysis 13

2.2 Global and biome forest AGB carbon stocks **13**

2.3 Spatial variability in forest AGB carbon density **15**

2.4 Factors and mechanism associated with the model-data discrepancy **19**

2.5 Conclusion **20**

2.1 References **22**

3. Post-fire biomass recovery offsets most fire carbon losses across global forests since 1990 ..... *25*

3.2 Method **26**

3.2.1 Harmonizing global forest disturbance and forest land-use change 26

3.2.2 Reconstructing post-disturbance biomass recovery 29

3.2.3 Modeling forest carbon dynamics using a spatially explicit bookkeeping model 32

3.3 Fire dominates disturbance-driven forest carbon losses **33**

3.4 Trends in gross fire carbon losses are primarily driven by carbon loss intensity **34**

3.5 Post-fire recovery offsets most fire-related carbon losses **35**

3.6 Fire contributes substantially to the full forest carbon budget **37**

3.7 Conclusion **38**

3.8 References **39**

LIST OF FIGURES

Figure 2-1 Comparison of AGC (carbon) estimates from ESA CCI Biomass data and CMIP6 ESM simulations. (a) Global-scale comparison. Solid bars show AGB within forest-dominated areas, while hatched bars indicate values for all regions without applying a forest mask. Red bars (with error bars) represent ESA CCI Biomass estimates and their associated uncertainty (standard deviation), whereas orange bars represent the CMIP6 multi-model ensemble (MME) mean. Numbers above the bars indicate the percentage bias of model estimates relative to the reference data. (b) Biome-level comparison across Köppen climate zones. Red bars denote ESA CCI Biomass estimates, orange bars show the CMIP6 MME mean, and individual points correspond to results from each model. Af, tropical rainforest; Am, tropical monsoon; Aw, tropical savanna; BW, desert; BS, semi-arid steppe; Cs, temperate dry summer; Cw, temperate dry winter; Cf, temperate without dry season; Ds, continental dry summer; Dw, continental dry winter; Df, continental without dry season; ET, tundra; and EF, ice cap. 15

Figure 2-2: Spatial patterns of forest AGB carbon density and model-data discrepancies. (a, b) The forest AGB carbon density spatial patterns of the ESA CCI Biomass dataset and the CMIP6 MME mean respectively. (c) The latitude pattern of model simulations and map data values. (d) The differences of model simulations and map data values. Red represents over-estimation, while blue represents under-estimation. (e) Agreement level among individual models regarding over- or under-estimation. This metric is defined as the proportion of individual ESMs for which the bias has the same sign as the bias of the MME. Darker shades indicate that more models share the same direction of bias. (f) The latitude pattern of model-data differences. 16

Figure 2-3. Taylor diagrams are used to evaluate CMIP6 ESM simulations against ESA CCI observations. (a) - (d) represent global and tropical, temperate, or boreal regions respectively, and each point represents a model. 17

Figure 2-4. ESMs were clustered into 4 groups based on KGE metrics. 18

Figure 2-5. (a) Feature importance of top 12 variables. The bar length represents feature importance, and the size of circle represents the relative magnitude of SHAP value. (b) Map of local dominant features. These features are identified based on their magnitude of SHAP values. Among them, "bio_17 (PDrQ)" (light blue), "wv0010_face" (brown color), "CanopyHeight" (dark green), and "ForestAge" (light green) are four dominant features at the global scale. Full variable names and descriptions are provided in Table 2-2. 19

Figure 2-6. Response curves of top 12 variables based on SHAP analysis. 20

Figure 3-1. Major biomes and regions considered in this study. 26

Figure 3-2. Performance of the recovery curves. AGB estimated from the recovery curves is compared with site-level AGB at corresponding ages and locations. AGB values are binned into 5-year forest-age intervals from 0–40 years and 10-year intervals for ages greater than 40 years for each forest biome. Dots represent mean AGB values from site-measured and modeled data derived from recovery curves. Error bars indicate the standard deviation. 31

Figure 3-3. Comparison of AGC accumulation rates during the first 0-30 years after regrowth with estimates from naturally regenerating forests reported by Cook-Patton et al. (2020) and Robinson et al. (2025). Regions shown correspond to those defined in Figure 3-1b. 31

Figure 3-4. Gross carbon losses from non-deforestation forest disturbances (1990–2020). (a, b) Cumulative above-ground carbon (AGC) losses and relative contributions of fire and non-fire disturbances across biomes (see also Figure S4). Values are aggregated over 1990–2020 (PgC), with fractions indicating the proportional contribution of each disturbance type. (c, d) Spatial distribution of mean annual gross carbon losses (Mg C ha^{-1} yr^{-1}) associated with fire (c) and non-fire (d) disturbances over the 30-year period. In regions lacking regional disturbance datasets (e.g., boreal Asia), non-fire disturbances are not quantified; in these areas, fire-related losses are derived solely from a global burned-area product (Methods). 34

Figure 3-5. Temporal trends in disturbance-related carbon losses, disturbed area, and loss intensity across biomes (2000–2020). (a–c) Annual gross above-ground carbon (AGC) losses from fire (orange) and non-fire (blue) disturbances. (d–f) Disturbed area associated with fire and non-fire events. (g–i) Carbon loss per unit

burned/disturbed area (loss intensity). Panels are organized by biome: boreal (a, d, g), temperate (b, e, h), and tropical (c, f, i). Solid lines denote statistically significant linear trends ($P < 0.05$), with slopes indicated, while dashed lines represent non-significant trends. 35

Figure 3-6. Carbon losses from fire and post-fire biomass recovery in forests affected by fires during 1990–2020. (a) Cumulative above-ground carbon (AGC) emissions from fire and corresponding post-fire biomass recovery gains over 1990–2020. Black points with error bars indicate the resulting net AGC change and associated standard errors. (b) Contribution of legacy effects to post-fire recovery by biome, showing the relative share (%) of biomass gains during 2005–2020 attributable to fires occurring in 1990–2005 ("older fires") and 2005–2020 ("recent fires"). (c) Spatial distribution of post-fire biomass recovery, expressed as mean annual carbon gain per unit area (Mg C ha^{-1} yr^{-1}) averaged over 1990–2020. (d) Spatial distribution of net fire-related forest biomass carbon change (Mg C ha^{-1} yr^{-1}) over 1990–2020, calculated as the balance between fire-induced carbon losses and post-fire recovery gains. 36

Figure 3-7. Spatial and temporal dynamics of forest carbon balance (1990–2020). (a–c) Temporal evolution of above-ground carbon (AGC) fluxes by biome. Bars represent annual carbon losses and gains from fire and non-fire disturbances, deforestation, afforestation, and growth in undisturbed forests. Black lines indicate the net AGC balance, calculated as the sum of all flux components. Panels correspond to boreal (a), temperate (b), and tropical (c) forests. (d) Spatial distribution of mean annual net AGC change (Mg C ha^{-1} yr^{-1}) over 1990–2020, integrating carbon losses from disturbances and deforestation with gains from post-disturbance recovery, growth in undisturbed forests, and afforestation. 37

Figure 3-8. Country-level comparison of deforestation-related AGC losses between this study and the BLUE bookkeeping model for 2000–2020 across (a) tropical, (b) temperate, and (c) boreal regions. The dashed line represents the 1:1 line. 38

LIST OF TABLES

Table 2-1 List of 30 CMIP6 ESMs used in this study 11

Table 2-2 List of environmental variable datasets. 12

Table 3-1 Disturbance datasets used in the analysis. 28

Table 3-2 Data sources used to delineate the forest land-use change and forest extent in 2020. 29

SYMBOLS AND ACRONYMS

AGB	Aboveground Biomass
AGC	Aboveground Carbon
BGB	Belowground Biomass
CAR	Climate Assessment Report
CCI	Climate Change Initiative
CLCD	China land cover dataset
CWD	Coarse Woody Debris
LCCMS	Landscape Change Monitoring System
EFDA	European Forest Disturbance Atlas
ESM	Earth System Models
ESA	European Space Agency
GABAM	Global Annual Burned Area Map
GFW	Global Forest Watch
KGE	Kling–Gupta Efficiency
LCCMS	Landscape Change Monitoring System
LUC	Land Use Change
LCCMS	Landscape Change monitoring System
LVOD	Volumetric Optical Depth
MME	Multi-Model Ensemble
PCA	Principal Component Analysis
TMF	Tropical Moist Forest
RMSE	Root Mean Square Error
SAR	Synthetic Aperture Radar
SHAP	SHapley Additive exPlanations

1 Summary

In the previous Climate Assessment Report (CAR) from Phase I, we addressed the use of the European Space Agency (ESA) Climate Change Initiative (CCI) Biomass data on the Above Ground Biomass (AGB; Mg ha^{-1}) of woody vegetation for evaluating TRENDYV8 DGVMs, the inference of tropical land carbon cycle parameters by combining CCI Biomass AGB estimates, L-band Volumetric Optical Depth (LVOD) from the Soil Moisture and Ocean Salinity (SMOS) mission, Leaf Area Index (LAI) data, and the change of tropical AGB inferred from LVOD calibrated to AGB, with a focus on the recovery of AGB from the most recent El Niño (Yang et al., 202x).

In the Phase II CAR, we used CCI Biomass AGB data to infer forest biomass changes in three regional studies: 1) forest biomass loss caused by plantation area expansion in Southeast Asia, 2) the deficit and loss of AGB across forest edges in Africa, and 3) the net carbon balance of boreal forests, with a focus on fire disturbances and post-fire AGB recovery.

In the Phase III CAR, we applied CCI Biomass AGB data to infer forest biomass losses and gains associated with fire, degradation, deforestation, and regrowth in tropical forests over the period 1990-2020. In this case study, we provided spatially explicit, long-term analysis of the carbon balance dynamics within disturbed tropical humid and dry forests, offering critical insights for can support national carbon inventories, REDD+ implementation, and targeted conservation planning.

In this Phase IV CAR, we applied CCI Biomass AGB data to assess forest carbon dynamics at both regional and global scales. For Europe, we combined inventory data, disturbance maps, and AGB estimates to evaluate changes in the forest carbon sink under increasing disturbance and harvest pressures. At the global scale, we integrated AGB data with long-term disturbance histories and regrowth dynamics to quantify carbon losses and gains in disturbed forests, highlighting strong regional differences in disturbance impacts and recovery processes.

In the initial version of the CAR from the CCI Biomass CCN phase, we evaluated forest AGB simulations from 30 CMIP6 Earth System Models (ESMs) under historical conditions using the 2020 ESA CCI Biomass product as a benchmark. The analysis assessed model performance at global and biome scales and investigated the key factors associated with model–data discrepancies. By combining model intercomparison, clustering analysis, and an explainable machine learning framework, we identified systematic biases in AGB simulations and linked them to differences in hydroclimatic conditions, vegetation structure, and model representations of ecosystem processes. This work provided a diagnostic basis for understanding model limitations and supports improvements in terrestrial carbon cycle projections. Building on the last phase's global analysis of disturbance-driven carbon losses and recovery, we extended the framework to include forest Land-Use Change (LUC) and the carbon gains from forests that are free of recorded disturbance since 1990, enabling more comprehensive accounting of forest AGC changes. We show that disturbances, particularly fires, play a central role in shaping forest carbon dynamics across biomes, with contrasting impacts depending on regional disturbance regimes and recovery capacity.

2 Evaluation of vegetation above-ground biomass carbon from CMIP6 ESMs using global satellite-based estimates

Vegetation dynamics, and for forests in particular, are a key component of the climate system through their control on carbon exchanges between land and atmosphere and the resulting feedbacks (Bar-On et al., 2018; Friedlingstein et al., 2025). As a result, enhancing forest extent and condition has been widely promoted as an effective nature-based mitigation pathway to strengthen terrestrial carbon uptake and support the objectives of the Paris Agreement (Federici et al., 2017; Griscom et al., 2017; Kaarakka et al., 2021). Forest Above Ground Biomass (AGB; Mg ha^{-1}) represents the main observable proxy of this carbon storage and displays strong spatial variability. This variability reflects the interplay between carbon accumulation processes, such as growth and recruitment, and loss processes including mortality, degradation, and decomposition (Reichstein & Carvalhais, 2019). Earth System Models (ESMs), such as those contributing to CMIP6, are extensively used to simulate and project these dynamics under different climate scenarios. Their outputs underpin assessments of future carbon sinks and are widely used in climate policy contexts (Flato, 2011; Prinn, 2013). However, projections remain highly uncertain, with substantial divergence across models, largely attributable to differences in process representation and parameterization. This underscores the need for systematic benchmarking to assess model fidelity and constrain uncertainties.

Robust model evaluation depends critically on the availability of consistent, large-scale observational datasets. Earlier efforts to map forest biomass relied primarily on optical satellite observations combined with field data (Ruesch & Gibbs, 2008; Baccini et al., 2012; Saatchi et al., 2011; Hu et al., 2016). While these approaches enabled global mapping, they suffer from well-known limitations, including sensitivity to cloud cover, signal saturation in higher biomass regions, and limited ability to capture woody biomass due to restricted canopy penetration. The ESA GlobBiomass dataset (Santoro et al., 2021) marked a significant improvement by providing a global AGB map for 2010 at 100 m resolution based on Synthetic Aperture Radar (SAR), which offers improved sensitivity to vegetation structure and reduced dependence on illumination and atmospheric conditions. Building on this, the ESA CCI Biomass product provides a temporally consistent AGB time series derived from multiple SAR sensors, using spaceborne LiDAR height measurements to constrain canopy-structure information within the SAR-based retrieval framework rather than directly calibrating AGB estimates with LiDAR biomass (Santoro et al., 2024). Independent validation against field and airborne observations indicates that the dataset reliably captures large-scale spatial patterns of AGB, although some regional biases persist due to methodological assumptions and reduced sensitivity of SAR signals at high biomass densities. Given these characteristics, the CCI Biomass dataset provides a suitable observational benchmark for evaluating ESM-derived biomass fields.

Here, we evaluate AGB simulations from CMIP6 ESMs over the historical period (2010–2014), with a focus on forest-dominated regions, using the CCI Biomass dataset as a reference. The analysis is designed to: (i) characterize model performance at global and biome scales and identify where discrepancies are largest, (ii) examine how differences in model structure contribute to biases in simulated biomass, and (iii) explore the environmental and climatic

controls associated with these discrepancies through a machine learning framework. The outcomes are intended to inform model development and improve the representation of vegetation carbon dynamics in future projections.

2.1 Method

2.1.1 ESA CCI Biomass dataset

The ESA CCI Biomass dataset (version 5; https://climate.esa.int/en/projects/biomass/; Santoro et al., 2024) provides spatially explicit estimates of above-ground biomass (AGB) of woody vegetation for 2010 and the period 2015–2021. These estimates are derived from the integration of multiple Synthetic Aperture Radar (SAR) observations, including data from Sentinel-1, Envisat ASAR, ALOS PALSAR, and ALOS-2 PALSAR-2 missions. The retrieval framework is further constrained using spaceborne LiDAR measurements from ICESat-2, together with ancillary information on vegetation cover and land cover (Santoro et al., 2024). The native spatial resolution of the dataset is 1 hectare. For the purpose of this analysis, the data were aggregated to a coarser grid by spatial averaging. We first used the 0.5° resolution products derived from the original dataset and subsequently aggregated them to a 1° × 1° grid to ensure consistency with the spatial resolution of the ESM outputs. AGB maps corresponding to the years 2010 and 2015 were selected for model evaluation. Sensitivity tests indicated that the choice of reference year had only a limited influence on the overall results. To account for uncertainties in the biomass estimates, the associated standard deviation layers provided with the dataset were included in the analysis. Finally, biomass values expressed in Mg ha^{-1} were converted to carbon density (MgC ha^{-1}) using a factor of 0.5 following Chave et al. (2005).

2.1.2 CMIP6 ESM simulations

Outputs from 30 CMIP6 Earth System Models (ESMs) under the historical experiment were used in this analysis (Table 2-1). Information on the land surface components associated with each model was obtained from the official CMIP6 documentation (https://wcrp-cmip.github.io/CMIP6_CVs/docs/CMIP6_source_id.html).

For each model, AGB carbon density was derived by subtracting root carbon (cRoot) from total vegetation carbon (cVeg). In cases where cRoot was not available, AGB was approximated as 80% of cVeg following Liu et al. (2015). Model outputs were taken from the r1i1p1f1 (r, i, p, and f denote the realization, initialization, physics, and forcing indices in the CMIP6 ensemble-member identifier, respectively) realization for most simulations, with the exception of UKESM1-0-LL and UKESM1-1-LL, for which r1i1p1f2 was used due to data availability constraints.

To ensure consistency with the observational benchmark and reduce the influence of interannual variability, we averaged monthly outputs over the period 2010–2014. All model fields were then regridded to a common 1° × 1° spatial resolution using a nearest-neighbor approach. Forest areas were defined based on the simulated tree fraction (treeFrac), with grid cells classified as forest where the multi-model mean tree fraction exceeded 50% at 1° resolution. For models lacking treeFrac output, the tree fraction was estimated from land cover fractions (landCoverFrac).

It should also be noticed that ESM biomass outputs generally do not provide formal uncertainty estimates at grid-cell or aggregated scales, despite being affected by uncertain parameters, process representations, and forcing inputs. Therefore, the comparison with CCI Biomass should

be interpreted as a diagnostic benchmark of model–data differences rather than a formal probabilistic test of model consistency with observations.

Table 2-1 List of 30 CMIP6 ESMs used in this study

No.	Name	Land model	Land model resolution (°)	cRoot data
1	ACCESS-ESM1-5	CABLE 2.4	1.24 × 1.88	Yes
2	BCC-CSM2-MR	BCC_AVIM 2	1.13 × 1.13	Yes
3	BCC-ESM1	BCC_AVIM 2	2.81 × 2.81	No
4	CanESM5	CLASS 3.6, CTEM 1.2	2.81 × 2.81	Yes
5	CESM2-FV2	CLM5	1.88 × 2.50	Yes
6	CESM2-WACCM-FV2	CLM5	1.88 × 2.50	Yes
7	CESM2-WACCM	CLM5	0.94 × 1.25	Yes
8	CESM2	CLM5	0.94 × 1.25	Yes
9	CMCC-CM2-SR5	CLM4.5	0.94 × 1.25	No
10	CMCC-ESM2	CLM4.5	0.94 × 1.25	No
11	CNRM-ESM2-1	ISBA+CTRIP	1.41 × 1.41	Yes
12	E3SM-1-1-ECA	ELM v1.1, MOSART v1.1	1.00 × 1.00	No
13	E3SM-1-1	ELM v1.1, MOSART v1.1	1.00 × 1.00	No
14	EC-Earth3-CC	HTESSEL, LPJ-GUESS v4	0.70 × 0.70	Yes
15	EC-Earth3-Veg-LR	HTESSEL, LPJ-GUESS v4	1.13 × 1.13	No
16	GFDL-ESM4	GFDL-LM 4.1	1.00 × 1.25	No
17	INM-CM4-8	INM-LND 1	1.50 × 2.00	No
18	INM-CM5-0	INM-LND 1	1.50 × 2.00	No
19	IPSL-CM6A-LR-INCA	ORCHIDEE v2.0	1.26 × 2.50	Yes
20	IPSL-CM6A-LR	ORCHIDEE v2.0	1.26 × 2.50	Yes
21	KIOST-ESM	NCAR-CLM 4	1.88 × 1.88	Yes
22	MPI-ESM-1-2-HAM	JSBACH 3.20	1.88 × 1.88	No
23	MPI-ESM1-2-LR	JSBACH 3.20	1.88 × 1.88	No
24	NorCPM1	CLM4	1.88 × 2.50	Yes
25	NorESM2-LM	CLM5	1.88 × 2.50	Yes
26	NorESM2-MM	CLM5	0.94 × 1.25	Yes
27	SAM0-UNICON	CLM4	0.94 × 1.25	No
28	TaiESM1	CLM4	0.94 × 1.25	Yes
29	UKESM1-0-LL	JULES-ES-1.0	1.25 × 1.88	Yes
30	UKESM1-1-LL	JULES-ES-1.0	1.25 × 1.88	Yes

2.1.3 Auxiliary datasets

To explore the environmental drivers underlying model–data discrepancies across regions, we compiled a set of auxiliary variables describing climate, soil, and vegetation conditions (Table 2-2). Climatic information was obtained from the WorldClim v2.1 dataset (Fick & Hijmans, 2017), from which 19 bioclimatic variables were extracted. Soil characteristics were derived from the SoilGrids 2.0 product (Poggio et al., 2021), including 13 variables describing soil texture and physicochemical properties. The original six soil depth layers were aggregated into two representative layers for this analysis: a surface layer (0–30 cm) and a deeper layer (30–200 cm).

Table 2-2 List of environmental variable datasets.

Type	Name	Description	Spatial resolution
Climate	bio1 (Tmean)	Annual Mean Temperature	10 × 10'
	bio2 (MDR)	Mean Diurnal Range	
	bio3 (ISO)	Isothermality (BIO2/BIO7*100)	
	bio4 (Tssn)	Temperature Seasonality	
	bio5 (Tmax)	Max Temperature of Warmest Month	
	bio6 (Tmin)	Min Temperature of Coldest Month	
	bio7 (TAR)	Temperature Annual Range	
	bio8 (TWeQ)	Mean Temperature of Wettest Quarter	
	bio9 (TDrQ)	Mean Temperature of Driest Quarter	
	bio10 (TWaQ)	Mean Temperature of Warmest Quarter	
	bio11 (TCoQ)	Mean Temperature of Coldest Quarter	
	bio12 (Prec)	Annual Precipitation	
	bio13 (PWM)	Precipitation of Wettest Month	
	bio14 (PDM)	Precipitation of Driest Month	
	bio15 (Pssn)	Precipitation Seasonality	
	bio16 (PWeQ)	Precipitation of Wettest Quarter	
	bio17 (PDrQ)	Precipitation of Driest Quarter	
	bio18 (PWaQ)	Precipitation of Warmest Quarter	
	bio19 (PCoQ)	Precipitation of Coldest Quarter	
Soil	bdod	Bulk density of the fine earth fraction	5 × 5 km
	cec	Cation Exchange Capacity of the soil	
	cfvo	Volumetric fraction of coarse fragments (> 2 mm)	
	clay	Proportion of clay particles (< 0.002 mm) in the fine earth fraction	
	nitrogen	Total nitrogen (N)	
	ocd	Organic carbon density	
	phh2o	Soil pH	
	sand	Proportion of sand particles (> 0.05/0.063 mm) in the fine earth fraction	
	silt	Proportion of silt particles (≥ 0.002 mm and ≤ 0.05/0.063 mm) in the fine earth fraction	
	soc	Soil organic carbon content in the fine earth fraction	
	wv0010	Volumetric Water Content at 10 kPa suction	
	wv0033	Volumetric Water Content at 33 kPa suction	
	wv1500	Volumetric Water Content at 1500 kPa suction	
Vegetation	CanopyHeight	Canopy Height (m)	10 × 10 km
	ForestAge	Forest Age (years)	1 × 1 km
	TreeDensity	Tree Density	1 × 1 km

2.1.4 Statistical analysis

To assess model performance and examine the role of model structure and parameterization in shaping these differences, we implemented a two-step analytical framework.

In the first step, model performance was quantified using the Kling–Gupta Efficiency (KGE) metric across four spatial domains: global, tropical, temperate, and boreal regions. KGE (Gupta & Kling, 2011) summarizes model–observation agreement by combining three complementary components—correlation (r), bias ratio (β), and variability ratio (γ)—into a single metric (Eq. 1), thereby enabling a balanced assessment of errors in spatial pattern, mean magnitude, and variability. KGE values are bounded above by 1, with higher values indicating better agreement with the reference dataset. In the second step, we applied an unsupervised clustering approach to group models according to their performance characteristics. Specifically, an agglomerative hierarchical clustering algorithm was used to partition the ensemble of ESMs into k clusters based on their KGE scores. Although the silhouette analysis suggested an optimal solution at k = 5, we selected k = 4 as the final configuration to achieve a balance between statistical robustness and interpretability.

$$KGE = 1 - \sqrt{(r-1)^2 + (\beta\text{-}1)^2 + (\gamma\text{-}1)^2} \quad \text{(Eq.1)}$$

where r denotes the correlation coefficient, β represents the bias ratio and γ corresponds to the variability ratio.

To further investigate the drivers of model–data discrepancies in forest AGB carbon density, we implemented a Random Forest regression framework using the previously described environmental variables as predictors. The target variable was defined as the spatial difference between the multi-model ensemble (MME) mean of CMIP6 simulations and the ESA CCI Biomass reference dataset at the pixel level.

The dataset was randomly partitioned into training (80%) and testing (20%) subsets to evaluate model performance and generalization. Hyperparameter tuning focused on the number of trees (n_estimators), which was varied between 50 and 400. Model performance showed limited improvement beyond 200 trees; therefore, n_estimators was set to 200, while all other parameters were kept at their default settings.

To interpret the model outputs, we applied SHapley Additive exPlanations (SHAP) analysis to quantify both the relative importance and directional influence of each predictor. The dominant explanatory factors for model–data discrepancies were identified at the pixel level based on the magnitude of their SHAP values. All analyses were conducted using Python 3.12, with implementations from the scikit-learn and shap libraries.

2.2 Global and biome forest AGB carbon stocks

At the global scale, the ESA CCI Biomass dataset indicates a total AGB carbon stock of 285.7 PgC. When the analysis is restricted to forest-dominated areas (defined as grid cells with a multi-model mean tree fraction exceeding 50%; see Methods), this estimate decreases to 200.9 PgC. This masking step is required because the CCI Biomass product represents woody vegetation only (Santoro et al., 2024), whereas ESM outputs include all vegetation types, leading to systematic overestimation in regions dominated by non-forest cover (Figure S2).

Across the 30 CMIP6 models, the MME mean estimates global forest AGB carbon at 241.3 PgC, with a substantial inter-model standard deviation of 72.7 PgC (Figure 1a). Relative to the observational benchmark, this corresponds to an average positive bias of 40.4 PgC (approximately 20%), indicating a general tendency toward overestimation. Model spread remains large, with inter-model variability equivalent to roughly 30% of the ensemble mean. Among individual models, SAM0-UNICON and ACCESS-ESM1-5 show the strongest positive biases (81% and 71%, respectively), whereas BCC-CSM2-MR, E3SM-1-1-ECA, EC-Earth3-Veg-LR, IPSL-CM6A-LR-INCA, and MPI-ESM1-2-LR remain within 10% of the reference estimate.

Model performance in predicting forest AGB varies considerably across regions. To investigate this spatial heterogeneity, we evaluated model performance across 13 climatic zones, defined by the Köppen classification system to represent diverse thermal and hydrological conditions. As shown in Figure 1b, the MME mean indicates that most biomes are characterized by positive biases, particularly in humid and seasonally dry tropical regions, whereas underestimation occurs in only a limited number of biomes (BW, Cs, and Ds) and remains small in magnitude (< 0.5 PgC). The tropical rainforest (Af) biome contributes the largest share to the global bias, with an average overestimation of 19.2 PgC (31%).

At the model level, performance varies considerably across biomes. For instance, SAM0-UNICON and E3SM-1-1 exhibit their largest positive biases in tropical regions, whereas ACCESS-ESM1-5 and CNRM-ESM2-1 show stronger overestimation in boreal and temperate humid zones. Importantly, regional biases within specific biomes, particularly those with high biomass, often exceed the corresponding global mean bias of each model. This indicates that compensating errors (i.e., the cancellation of over- and under-estimations across different biomes) across regions can obscure substantial regional discrepancies in global assessments. These results highlight the importance of evaluating model performance at biome or regional scales to better diagnose model deficiencies and guide targeted improvements.

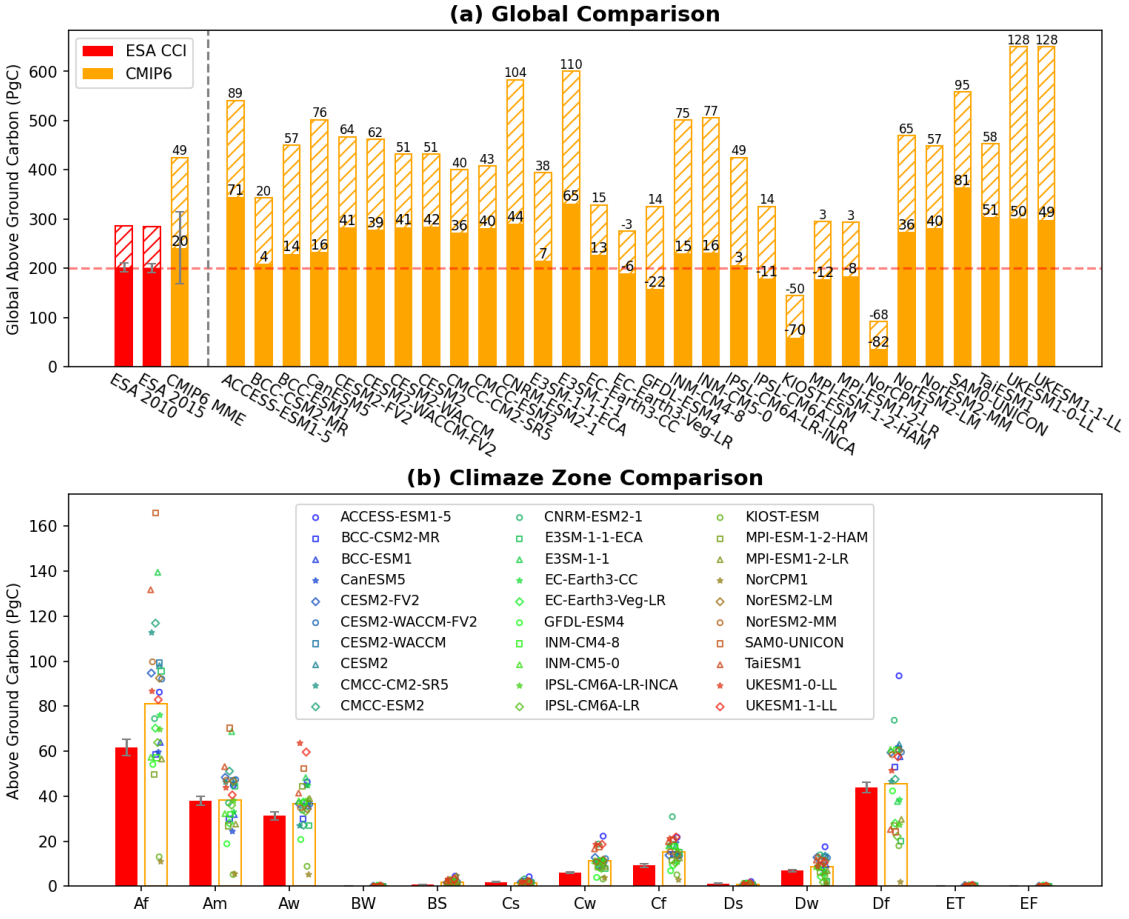

Figure 2-1 Comparison of AGC (carbon) estimates from ESA CCI Biomass data and CMIP6 ESM simulations. (a) Global-scale comparison. Solid bars show AGB within forest-dominated areas, while hatched bars indicate values for all regions without applying a forest mask. Red bars (with error bars) represent ESA CCI Biomass estimates and their associated uncertainty (standard deviation), whereas orange bars represent the CMIP6 multi-model ensemble (MME) mean. Numbers above the bars indicate the percentage bias of model estimates relative to the reference data. (b) Biome-level comparison across Köppen climate zones. Red bars denote ESA CCI Biomass estimates, orange bars show the CMIP6 MME mean, and individual points correspond to results from each model. Af, tropical rainforest; Am, tropical monsoon; Aw, tropical savanna; BW, desert; BS, semi-arid steppe; Cs, temperate dry summer; Cw, temperate dry winter; Cf, temperate without dry season; Ds, continental dry summer; Dw, continental dry winter; Df, continental without dry season; ET, tundra; and EF, ice cap.

2.3 Spatial variability in forest AGB carbon density

The spatial distribution of forest AGB carbon density from the ESA CCI Biomass dataset and the CMIP6 MME mean (Figure 2-2) shows that both datasets capture similar large-scale patterns, with peak biomass densities (>100 MgC ha^{-1}) concentrated in equatorial humid regions and substantially lower values (~50 MgC ha^{-1}) in mid-latitude forests of both hemispheres. However, the spatial distribution of model–data differences (MME minus CCI Biomass) exhibits strong regional heterogeneity rather than a simple latitudinal structure.

Pronounced overestimation is particularly evident across East and Southeast Asia. In contrast, the Amazon and Congo basins show spatially heterogeneous biases, with positive deviations in their northwestern sectors and negative deviations in eastern regions. In boreal zones, models

tend to underestimate AGB across Siberia, whereas consistent overestimation is found in Canada and Eastern Europe. Analysis at the individual model level reveals that these biases are not random; approximately 67% of the models exhibit deviations in the same direction across nearly half (47%) of the evaluated regions (Figure 2-2e), indicating a systematic component in model behavior. Moreover, even when accounting for uncertainties in the CCI Biomass dataset, discrepancies exceeding three times the observational uncertainty occur across more than 75% of the regions, confirming the robustness of these spatial mismatch patterns.

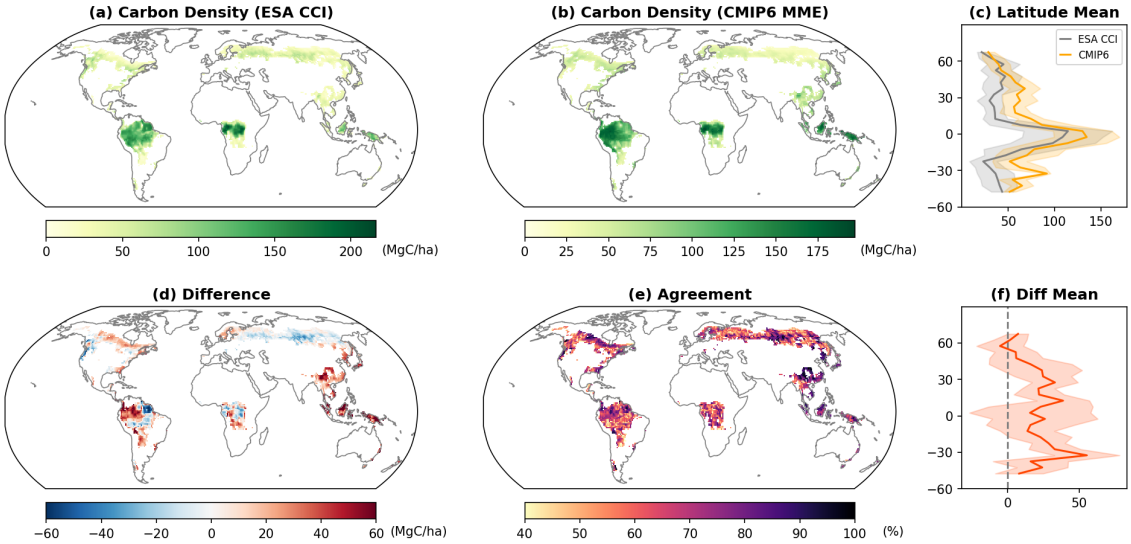

Figure 2-2: Spatial patterns of forest AGB carbon density and model-data discrepancies. (a, b) The forest AGB carbon density spatial patterns of the ESA CCI Biomass dataset and the CMIP6 MME mean respectively. (c) The latitude pattern of model simulations and map data values. (d) The differences of model simulations and map data values. Red represents over-estimation, while blue represents under-estimation. (e) Agreement level among individual models regarding over- or under-estimation. This metric is defined as the proportion of individual ESMs for which the bias has the same sign as the bias of the MME. Darker shades indicate that more models share the same direction of bias. (f) The latitude pattern of model-data differences.

Model performance is further assessed using Taylor diagrams (Taylor, 2001), which summarize spatial correlation, variability, and error characteristics at 1° resolution. As shown in Figure 2-3, most models reproduce the spatial pattern of AGB reasonably well, as indicated by relatively high correlation coefficients, particularly at the global scale and in tropical regions. However, they tend to overestimate the magnitude of spatial variability. The model performed worse in temperate and boreal regions, where both correlation and representation of variability are weaker.

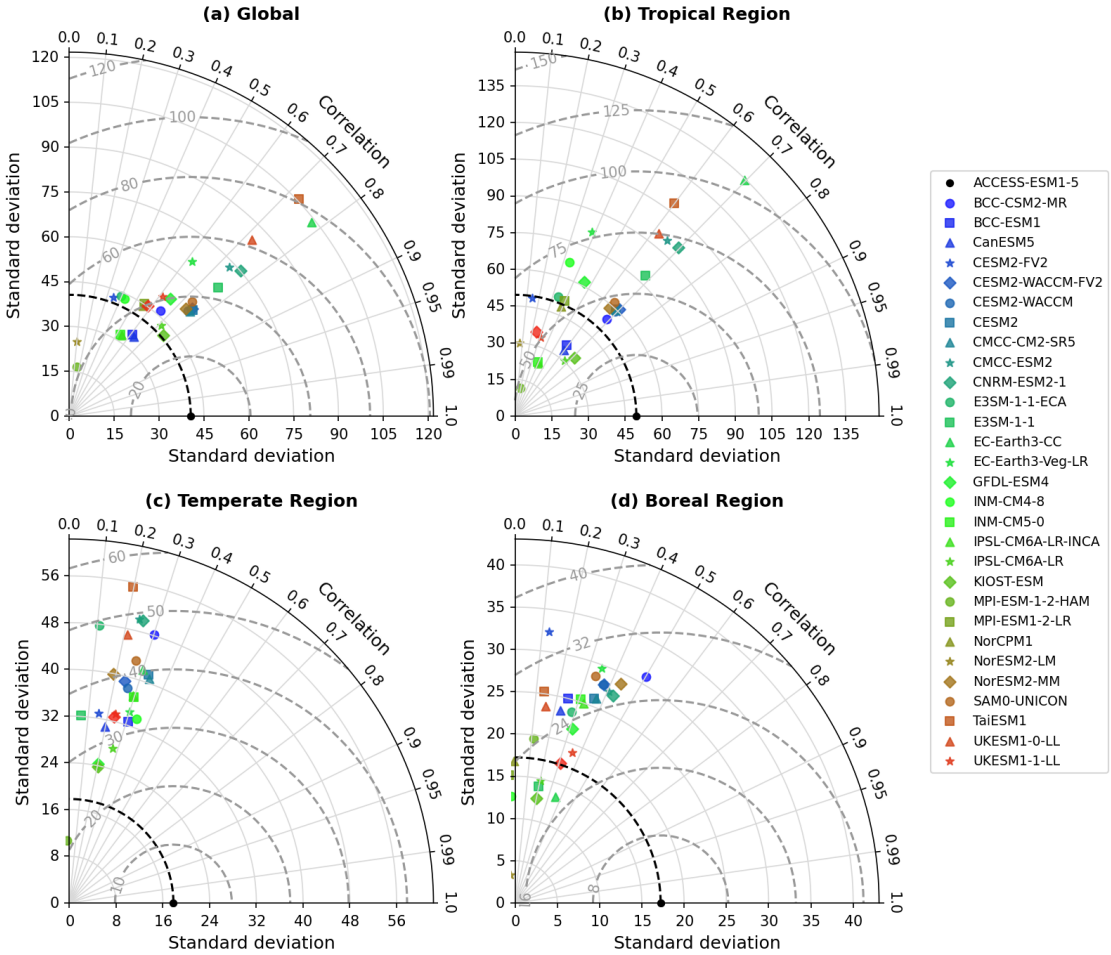

Figure 2-3. Taylor diagrams are used to evaluate CMIP6 ESM simulations against ESA CCI observations. (a) - (d) represent global and tropical, temperate, or boreal regions respectively, and each point represents a model.

These patterns are consistent with the Kling–Gupta Efficiency (KGE) results. KGE values are relatively high at the global scale and in tropical regions (around 0.63), but decrease markedly in temperate regions (to approximately 0.06). Both the Taylor diagrams and KGE metrics reveal clear groupings of models with similar performance characteristics. Such clustering suggests that shared structural features or parameterizations may underlie common biases, providing useful guidance for diagnosing sources of model divergence.

To provide an integrated view of model performance across spatial domains, we applied Principal Component Analysis (PCA) followed by clustering. The PCA was performed on four performance indicators—Kling–Gupta Efficiency (KGE) scores at the global, tropical, temperate, and boreal scales—and reduced them to two dominant components. The first principal component (PC1) mainly captures variability in performance across the global, tropical, and temperate regions, whereas the second component (PC2) reflects contrasting behavior, with positive loadings for temperate and boreal regions and negative associations with global and tropical performance (Figure 2-4). Together, these two components effectively summarize the main dimensions of inter-model differences among the 30 ESMs. The PCA results are interpreted here primarily as an exploratory diagnostic of inter-model differences. A future version will include the PC1–PC2 loadings for the four regional KGE indicators and the fraction of total variance explained by these components.

Based on these reduced dimensions, we grouped the models into four clusters (see Methods; Figure 2-4). The largest group (Group I, 19 models) shows relatively stable and consistent performance across all regions. Group II (2 models: KIOST-ESM and NorCPM1) is characterized by pronounced deficiencies in tropical regions. Group III (7 models: ACCESS-ESM1-5, CMCC-CM2-SR5, CMCC-ESM2, CNRM-ESM2-1, TaiESM1, UKESM1-0-LL, and UKESM1-1-LL) exhibits weaker performance in temperate and boreal zones. In contrast, Group IV (2 models: SAM0-UNICON and INM-CM5-0) performs poorly across all regions, resulting in the lowest overall model performance at the global scale.

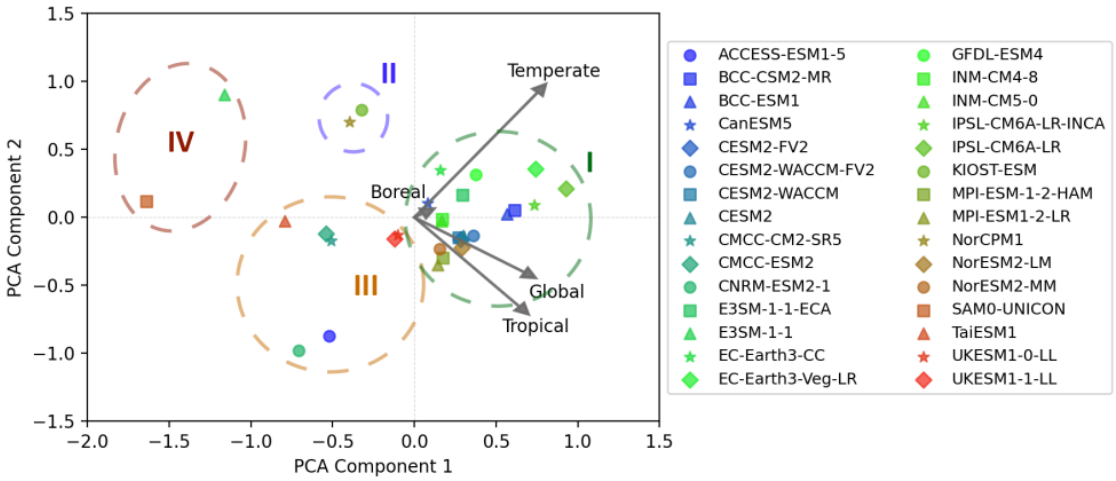

Figure 2-4. ESMs were clustered into 4 groups based on KGE metrics.

The clustering patterns in model performance appear to reflect underlying differences in land surface model configurations (Table 2-1). Models in Groups II and IV, which show weaker performance in tropical and boreal regions, are largely based on earlier land model versions, particularly CLM4 (e.g., SAM0-UNICON, KIOST-ESM, and NorCPM1). In contrast, models built on the updated CLM4.5 framework (e.g., CMCC-CM2-SR5 and CMCC-ESM2) are primarily assigned to Group III and exhibit intermediate skill, with improved performance in temperate and boreal regions but remaining limitations in the tropics. The highest-performing models (Group I) predominantly rely on the more recent CLM5 configuration, including several CESM variants, and show more consistent performance across all climatic zones.

Beyond differences in model versions, the representation of key ecological processes also emerges as an important factor. Models that omit processes, such as nitrogen cycling and dynamic vegetation (e.g., CNRM-ESM2-1 and INM-CM5-0), tend to perform poorly and particularly in tropical regions (Gier et al., 2024). However, the inclusion of these processes alone is not sufficient to ensure improved performance. For instance, although the JULES-ES configuration used in UKESM1-1-LL includes a nitrogen cycle, its limited sensitivity of productivity to nitrogen availability constrains its overall impact (Davies-Barnard et al., 2020), which may explain the model's weak performance in tropical regions. Similarly, ACCESS-ESM1-5 accounts for both nitrogen and phosphorus limitations but still exhibits substantial biases in the tropics.

These results indicate that model performance is not determined solely by the presence of advanced process representations, but also by how effectively these processes are parameterized and coupled within the land model. Accurate simulation of vegetation dynamics and nutrient constraints therefore depends on both process inclusion and their functional implementation.

2.4 Factors and mechanism associated with the model-data discrepancy

To identify the environmental drivers of model–data discrepancies, we applied a Random Forest (RF) regression model using the compiled environmental variables as predictors and the spatial differences between model simulations and observational data as the target (see Methods; Figure 2-5a). The RF model showed strong performance, with a coefficient of determination (R^2) of 0.97 and an RMSE of 4.17 for the training data, and retained good predictive skill on the independent test set (R^2 = 0.79; RMSE = 11.58). These results indicate that the model effectively captures the main controls on spatial variability in model–data differences.

Feature importance analysis was then used to quantify the relative contribution of different environmental factors (Figure 2-5a). Climate-related variables emerged as the dominant drivers, explaining 44.8% of the variance, followed by soil properties (34.8%). Vegetation structural characteristics—represented by tree height, forest age, and tree density—accounted for 20.4% of the variation, despite being described by a smaller set of predictors. Within this category, canopy height played a particularly important role and was the single most influential variable overall, contributing 14.3% to the explained variance.

Among the climatic variables, those associated with water availability showed consistently high importance, indicating that hydroclimatic conditions are a key factor controlling the spatial patterns of model–data discrepancies.

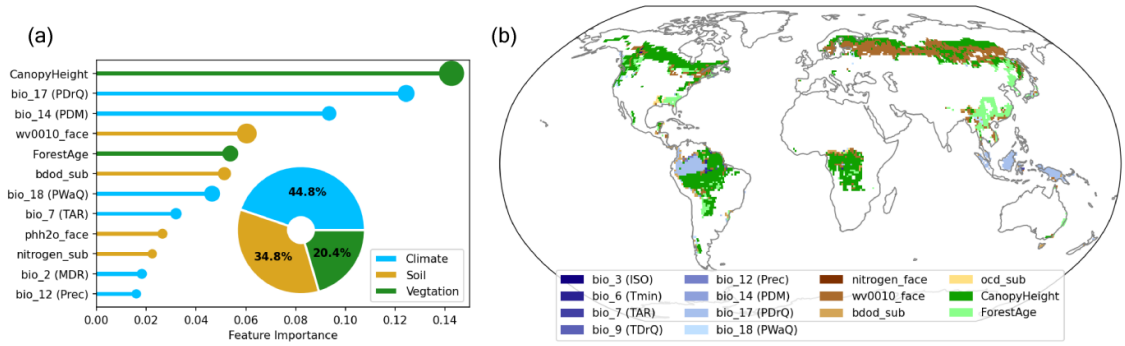

Figure 2-5. (a) Feature importance of top 12 variables. The bar length represents feature importance, and the size of circle represents the relative magnitude of SHAP value. (b) Map of local dominant features. These features are identified based on their magnitude of SHAP values. Among them, "bio_17 (PDrQ)" (light blue), "wv0010_face" (brown color), "CanopyHeight" (dark green), and "ForestAge" (light green) are four dominant features at the global scale. Full variable names and descriptions are provided in Table 2-2.

Figure 2-5b illustrates the dominant environmental controls on model–data discrepancies at the local scale, complemented by SHAP dependence relationships (Figure 2-6) that provide insight into the underlying mechanisms of biomass prediction biases.

Canopy height emerges as a key determinant across several regions, including the northeastern and southern Amazon, the Congo Basin, and northern Canada. In tropical humid regions such as the Amazon and Congo, model underestimation is most pronounced in areas characterized by tall canopies. In contrast, in northern Canada, overestimation tends to occur in regions with relatively low canopy height. The systematic underestimation in tall tropical forests likely reflects

the inability of current models to adequately represent complex vertical structure and associated biomass accumulation.

Forest age represents another important control, particularly in southern China, where extensive young plantations are present. In these regions, models tend to overestimate biomass, suggesting that insufficient representation of stand age and successional dynamics can lead to inflated carbon stock estimates in younger forests.

Water availability also plays a dominant role in shaping discrepancies, especially in the northwestern Amazon, Southeast Asia, and boreal Siberia. In Siberia, model underestimation is associated with areas of higher soil moisture in the upper soil layers. Conversely, in the northwestern Amazon and Southeast Asia, persistent overestimation occurs under humid conditions with abundant precipitation. These patterns suggest that models may overstate the positive influence of water availability on vegetation growth, potentially due to insufficient representation of other limiting factors such as nutrient availability or light competition.

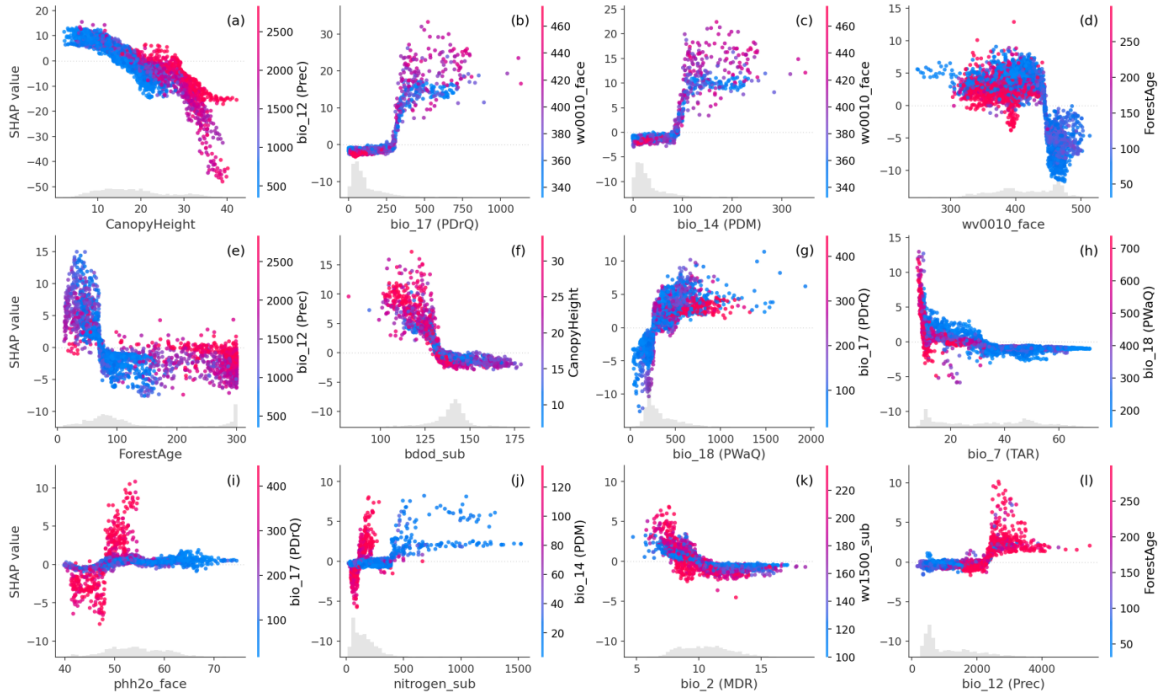

Figure 2-6. Response curves of top 12 variables based on SHAP analysis.

2.5 Conclusion

Our analysis identifies a consistent positive bias in CMIP6 ESM simulations of forest AGB relative to the ESA CCI Biomass dataset, amounting to an overestimation of approximately 20% at the global scale, together with substantial inter-model variability. This discrepancy is not spatially uniform but exhibits pronounced regional contrasts. In the tropics, models strongly overestimate AGB in East and Southeast Asia, whereas the Amazon and Congo basins display heterogeneous patterns, with positive biases in their northwestern regions and negative biases toward the east. In extratropical regions, AGB is generally underestimated across Siberia but overestimated in Canada and Eastern Europe.

These spatial patterns are closely associated with differences in the representation of key biogeochemical and ecological processes. At the global scale, models incorporating more advanced treatments of nutrient limitation and vegetation dynamics tend to show improved agreement with observational estimates. Complementary machine learning analysis further isolates the dominant environmental controls on local discrepancies, highlighting the roles of hydroclimatic conditions and vegetation structural characteristics.

Specifically, models tend to underestimate biomass in tall, structurally complex tropical forests, overestimate biomass in regions dominated by young plantations, and misrepresent biomass responses to water availability in areas with high soil moisture or deep water tables. This underestimation is likely conservative because CCI Biomass itself tends to underestimate AGB in high-biomass forests, particularly where C- and L-band SAR backscatter exhibits reduced sensitivity or saturation at high biomass levels and where generic canopy-structure constraints may not fully represent dense, structurally complex tropical forests (Santoro et al., 2024; ESA CCI Biomass ATBD/PVIR). Therefore, the true magnitude of model underestimation in structurally complex tropical forests may be larger than indicated by the model–CCI Biomass comparison. At the same time, CCI Biomass should be interpreted as an observation-based reference product rather than an error-free ground truth, as its AGB estimates include retrieval and validation uncertainties. Together, these findings indicate that improving the representation and interaction of vegetation structure, nutrient constraints, and water-related processes is essential for enhancing the reliability of future ESM projections of the terrestrial carbon cycle.

2.1 References

Baccini, A., S. J. Goetz, W. S. Walker, et al. 2012. "Estimated carbon dioxide emissions from tropical deforestation improved by carbon-density maps." Nature Climate Change 2(3): 182-185. https://doi.org/10.1038/nclimate1354

Bar-On, Y. M., R. Phillips, and R. Milo. 2018. "The biomass distribution on Earth." Proceedings of the National Academy of Sciences 115(25): 6506-6511. https://www.pnas.org/doi/abs/10.1073/pnas.1711842115

Besnard, S., S. Koirala, M. Santoro, et al. 2021. "Mapping global forest age from forest inventories, biomass and climate data." Earth Syst. Sci. Data 13(10): 4881-4896. https://essd.copernicus.org/articles/13/4881/2021/

Chave, J., C. Andalo, S. Brown, et al. 2005. "Tree allometry and improved estimation of carbon stocks and balance in tropical forests." Oecologia 145(1): 87-99. https://doi.org/10.1007/s00442-005-0100-x

Crowther, T. W., H. B. Glick, K. R. Covey, et al. 2015. "Mapping tree density at a global scale." Nature 525(7568): 201-205. https://doi.org/10.1038/nature14967

Davies-Barnard, T., J. Meyerholt, S. Zaehle, et al. 2020. "Nitrogen cycling in CMIP6 land surface models: progress and limitations." Biogeosciences 17(20): 5129-5148. https://bg.copernicus.org/articles/17/5129/2020/

Erb, K.-H., T. Kastner, C. Plutzar, et al. 2018. "Unexpectedly large impact of forest management and grazing on global vegetation biomass." Nature 553(7686): 73-76. https://doi.org/10.1038/nature25138

Federici, S., D. Lee, and M. Herold. 2017. "Forest mitigation: A permanent contribution to the paris agreement." WorNing Pap: 1-24.

Fick, S. E., and R. J. Hijmans. 2017. "WorldClim 2: new 1km spatial resolution climate surfaces for global land areas." International Journal of Climatology 37(12): 4302-4315.

Flato, G. M. 2011. "Earth system models: an overview." WIREs Climate Change 2(6): 783-800. https://wires.onlinelibrary.wiley.com/doi/abs/10.1002/wcc.148

Friedlingstein, P., M. O'Sullivan, M. W. Jones, et al. 2025. "Global Carbon Budget 2024." Earth Syst. Sci. Data 17(3): 965-1039. https://essd.copernicus.org/articles/17/965/2025/

Gier, B. K., M. Schlund, P. Friedlingstein, et al. 2024. "Representation of the terrestrial carbon cycle in CMIP6." Biogeosciences 21(22): 5321-5360. https://bg.copernicus.org/articles/21/5321/2024/

Griscom, B. W., J. Adams, P. W. Ellis, et al. 2017. "Natural climate solutions." Proceedings of the National Academy of Sciences 114(44): 11645-11650. https://www.pnas.org/doi/abs/10.1073/pnas.1710465114

Hansen, M. C., P. V. Potapov, R. Moore, et al. 2013. "High-Resolution Global Maps of 21st-Century Forest Cover Change." Science 342(6160): 850-853. https://www.science.org/doi/abs/10.1126/science.1244693

Hu, T., Y. Su, B. Xue, et al. 2016. "Mapping Global Forest Aboveground Biomass with Spaceborne LiDAR, Optical Imagery, and Forest Inventory Data." Remote Sensing 8(7): 565. https://www.mdpi.com/2072-4292/8/7/565

Kaarakka, L., M. Cornett, G. Domke, T. Ontl, and L. E. Dee. 2021. "Improved forest management as a natural climate solution: A review." Ecological Solutions and Evidence 2(3): e12090. https://besjournals.onlinelibrary.wiley.com/doi/abs/10.1002/2688-8319.12090

Lang, N., W. Jetz, K. Schindler, and J. D. Wegner. 2023. "A high-resolution canopy height model of the Earth." Nature Ecology & Evolution 7(11): 1778-1789. https://doi.org/10.1038/s41559-023-02206-6

Liu, Y. Y., A. I. J. M. van Dijk, R. A. M. de Jeu, et al. 2015. "Recent reversal in loss of global terrestrial biomass." Nature Climate Change 5(5): 470-474. https://doi.org/10.1038/nclimate2581

Negrón-Juárez, R. I., C. D. Koven, W. J. Riley, R. G. Knox, and J. Q. Chambers. 2015. "Observed allocations of productivity and biomass, and turnover times in tropical forests are not accurately represented in CMIP5 Earth system models." Environmental Research Letters 10(6): 064017. https://dx.doi.org/10.1088/1748-9326/10/6/064017

Poggio, L., L. M. de Sousa, N. H. Batjes, et al. 2021. "SoilGrids 2.0: producing soil information for the globe with quantified spatial uncertainty." SOIL 7(1): 217-240. https://soil.copernicus.org/articles/7/217/2021/

Prinn, R. G. 2013. "Development and application of earth system models." Proceedings of the National Academy of Sciences 110(supplement_1): 3673-3680. https://www.pnas.org/doi/abs/10.1073/pnas.1107470109

Reichstein, M., and N. Carvalhais. 2019. "Aspects of Forest Biomass in the Earth System: Its Role and Major Unknowns." Surveys in Geophysics 40(4): 693-707. https://doi.org/10.1007/s10712-019-09551-x

Ruesch, A., and H. K. Gibbs. 2008. "New IPCC Tier-1 global biomass carbon map for the year 2000." Available online from the Carbon Dioxide Information Analysis Center [http://cdiac. ornl. gov], Oak Ridge National Laboratory, Oak Ridge, Tennessee.

Saatchi, S. S., N. L. Harris, S. Brown, et al. 2011. "Benchmark map of forest carbon stocks in tropical regions across three continents." Proceedings of the National Academy of Sciences 108(24): 9899-9904. https://www.pnas.org/doi/abs/10.1073/pnas.1019576108

Santoro, M., O. Cartus, N. Carvalhais, et al. 2021. "The global forest above-ground biomass pool for 2010 estimated from high-resolution satellite observations." Earth Syst. Sci. Data 13(8): 3927-3950. https://essd.copernicus.org/articles/13/3927/2021/

Santoro, M., O. Cartus, S. Quegan, et al. 2024. "Design and performance of the Climate Change Initiative Biomass global retrieval algorithm." Science of Remote Sensing 10: 100169. https://www.sciencedirect.com/science/article/pii/S2666017224000531

Tian, L., X. Wu, Y. Tao, et al. 2023. "Review of Remote Sensing-Based Methods for Forest Aboveground Biomass Estimation: Progress, Challenges, and Prospects." Forests 14(6): 1086. https://www.mdpi.com/1999-4907/14/6/1086

Yang, C.-E., J. Mao, F. M. Hoffman, et al. 2018. "Uncertainty Quantification of Extratropical Forest Biomass in CMIP5 Models over the Northern Hemisphere." Scientific Reports 8(1): 10962. https://doi.org/10.1038/s41598-018-29227-7

Yang, H., Ciais, P., Frappart, F., Li, X., Brandt, M., Fensholt, R., ... & Wigneron, J. P. 2023. Global increase in biomass carbon stock dominated by growth of northern young forests over past decade. *Nature Geoscience*, *16*(10), 886-892. https://doi.org/10.1038/s41561-023-01274-4

3. Post-fire biomass recovery offsets most fire carbon losses across global forests since 1990

Global forests constitute the largest terrestrial carbon sink (Friedlingstein et al., 2025), yet both the magnitude and spatial distribution of this sink remain highly uncertain (Randerson et al., 2025; Bar-On et al., 2025). A major source of this uncertainty arises from the incomplete or inaccurate representation of disturbance-driven carbon losses and the subsequent regrowth processes in global models (Dye et al., 2024; O'Sullivan et al., 2024). The persistence of the forest carbon sink is increasingly challenged by intensifying natural disturbances—including fire, drought, and insect outbreaks—as well as direct anthropogenic pressures such as deforestation and timber harvest (Jones et al., 2024; Anderegg et al., 2020; Seidl et al., 2017). Quantifying both the immediate carbon losses from disturbances and the longer-term recovery dynamics is therefore essential for assessing the stability of forest carbon storage and its future role in climate mitigation.

Disturbance characteristics, including type, location, and severity, strongly influence both the magnitude of biomass loss and the trajectory of post-disturbance recovery (Lapola et al., 2023). For instance, clear-cut harvesting typically removes most above-ground biomass, resulting in large and immediate carbon losses. In contrast, many boreal fires only partially combust live biomass, with additional emissions occurring over extended periods through the decomposition of fire-induced dead organic matter (van Bellen et al., 2010; Izbicki et al., 2023). Recovery times also vary substantially, with boreal forests generally exhibiting slower regrowth compared to fire-adapted dry tropical systems (Palviainen et al., 2020; Poorter et al., 2016). Recent efforts have improved estimates of disturbance-related carbon losses by combining satellite-derived disturbance information with spatial biomass datasets (Grassi et al., 2023; Gibbs et al., 2025; Harris et al., 2021). However, post-disturbance recovery remains inconsistently represented due to methodological uncertainties. Existing approaches range from fixed recovery factors (IPCC, 2006), to biome-level recovery curves derived from satellite data (Heinrich et al., 2023; Holcomb et al., 2023), to statistical models based on field observations with limited spatial coverage (Robinson et al., 2025; Poorter et al., 2021). The absence of spatially explicit, observation-based recovery estimates across all forest types therefore constrains our ability to robustly quantify disturbance-driven carbon dynamics at the global scale.

In this study, we formed a global, 30 m forest disturbance dataset by integrating multiple regional Landsat-based products (Hermosilla et al., 2019; Liu et al., 2023; Qiu et al., 2025; Viana-Soto and Senf, 2025; Long et al., 2019; Vancutsem et al., 2021), with disturbances harmonized into fire and non-fire categories over the period 1990–2020. Disturbances are defined here as biomass-reducing events within forests that do not result in permanent land-use conversion and are therefore followed by regrowth. This dataset is combined with the spatially explicit forest carbon bookkeeping framework of Xu et al. (2026), which integrates time-varying disturbance information with a global set of gridded biomass recovery curves. This approach enables the tracking of carbon losses—including delayed emissions from dead biomass—and subsequent recovery at 30 m resolution over the past three decades. Recovery trajectories are estimated at a 1° grid scale using a space-for-time approach (Methods). Using this framework, we first disentangle the contributions of disturbance area, carbon loss intensity (i.e., carbon loss per unit disturbed area), and post-disturbance recovery to the net forest carbon balance. We then construct a global forest carbon budget by additionally accounting for carbon changes in undisturbed forests and fluxes associated with land-use transitions, including deforestation and

reforestation (Methods). This integrated analysis addresses key limitations in existing global carbon accounting approaches and provides new insights into whether forest disturbances over the past 30 years have remained largely compensated by recovery or have led to a sustained increase in net carbon losses.

3.2 Method

3.2.1 Harmonizing global forest disturbance and forest land-use change

We constructed a global, spatially explicit forest disturbance dataset at 30 m resolution by integrating six regional Landsat-based products covering Canada (Hermosilla et al., 2019), Europe (Viana-Soto and Senf, 2025), the conterminous United States (Qiu et al., 2025), China (Liu et al., 2023), the tropics (Vancutsem et al., 2021), and Australia (National Forest and Sparse Woody Vegetation Dataset, v8) (Table 3-1). Disturbance categories from these datasets were harmonized into two broad classes: fire and non-fire disturbances. In this framework, disturbances refer to events occurring within existing forest stands that reduce biomass but are followed by regrowth, and are therefore distinct from land-use changes that result in permanent forest conversion. In regions where Landsat-based disturbance records are not available (e.g., "Other boreal" and "Other regions", Figure 3-1b), fire disturbances were identified using a global burned-area dataset at 30 m resolution (Long et al., 2019). Comparable datasets for non-fire disturbances with similar temporal coverage are not currently available in these regions.

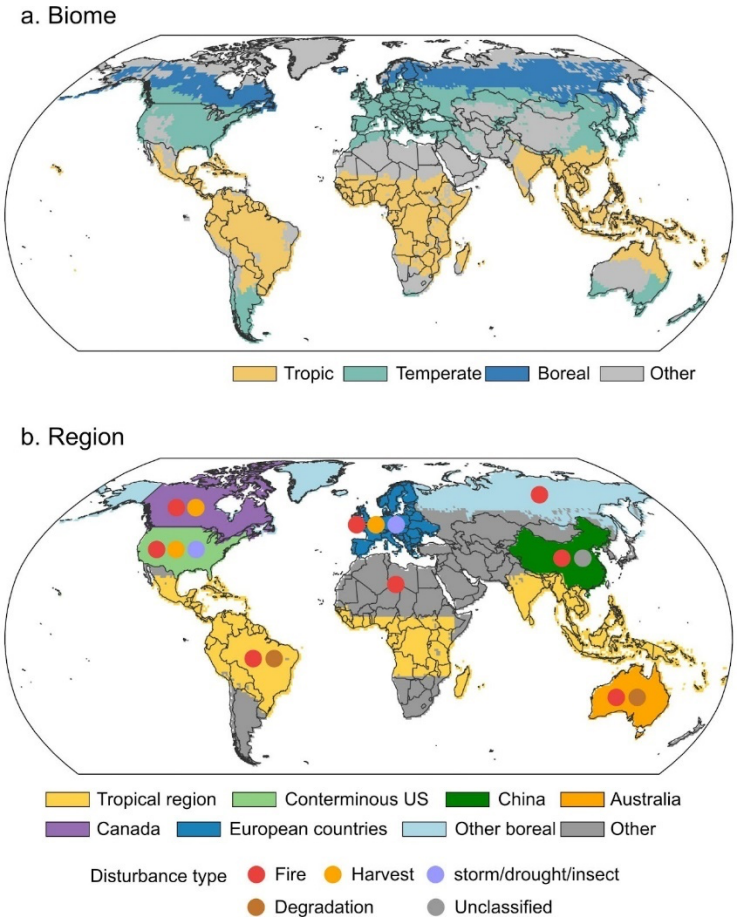

Figure 0-1. Major biomes and regions considered in this study.

Table 3-1 Disturbance datasets used in the analysis

Region	Time Period	Original type	Harmonized disturbance type	Dataset Name	Reference
Canada	1985-2020	Harvest, fire	Fire, Non-fire	Canada's disturbance datasets	Hermosilla et al. (2019)
Europe	1985-2023	Wind/bark beetle, fire, harvest	Fire, Non-fire	European Forest Disturbance Atlas (EFDA)	Viana-Soto and Senf (2025)
US	1988-2022	Fire, logging, stress, wind,construction, agricultural, water	Fire, Non-fire	Land Disturbance across the Conterminous United States	Qiu et al., (2025)
China	1986-2022	Fire, other	Fire, Non-fire	China's disturbance datasets	Liu et al., (2023)https://paperpile.com/c/QmnpoD/SkPg
Tropics	1990-2023	Degradation, deforestation, Regrowth. Fire	Humid: Fire, Non-fire Dry: Fire	Tropical Moist Forest (TMF) Global Annual Burned Area datasets	Vancutsem et al., (2021) Long et al., (2021)
Australia	1988-2023	Original land cover class: woody, forest, other	Fire, Non-fire (forest loss/gain)	National Forest and Sparse Woody Vegetation Data	Department of Climate Change, Energy, the Environment and Water (2023) Long et al., (2021)
Other boreal/ Other	1985-2021	Burned area	Fire	Global Annual Burned Area datasets (GABAM)	Long et al., (2021)

Forest land-use change (LUC), including deforestation and afforestation/reforestation, was primarily derived from annual regional land-cover change products (Table 3-2). In humid tropical regions, deforestation is directly represented within the Tropical Moist Forest (TMF) dataset. Deforestation was defined as transitions from forest to non-forest land cover, while afforestation and reforestation correspond to transitions in the opposite direction. For regions lacking temporally explicit LUC datasets (e.g., parts of the Russian boreal zone; Table 3-2), we reconstructed LUC transitions using a combination of global forest loss and gain datasets and thematic land-use products. Forest loss after 2000 was identified using the Landsat-based global forest cover loss dataset of Hansen et al. (2013), while forest loss during 1990–2000 was derived from Townshend et al. (2017). To distinguish permanent deforestation from temporary canopy disturbances, we overlaid forest loss pixels with 2020 cropland (Potapov et al. 2022), pasture (Parente et al. 2024), and oil palm (Descals et al. 2024) maps. Pixels that transitioned from forest to these land-use classes were classified as deforested and assumed to represent permanent land conversion. We adopted this because agricultural expansion (cropland, livestock grazing, and oil palm plantations) accounts for approximately 90% of global deforestation (FAO, 2022). Future refinements could further distinguish broad land-cover conversions, such as forest-to-cropland, forest-to-pasture, or forest-to-urban transitions, from vegetation-structure modifications in which land remains

vegetated but shifts from woody to herbaceous or shrub-dominated cover. Afforestation and reforestation were identified using global tree cover gain products (Hansen et al., 2013; Townshend et al., 2017), restricted to areas previously classified as non-forest.

Table 3-2. Data sources used to delineate forest land-use change and extent in 2020

Region	Forest in 2020	Forest land-use change	Time period	Data source	Reference
Canada	Coniferous Broad Leaf Mixedwood	Conversion between Forest and other Non-Forest classes	1984-2020	Annual forest land cover maps for Canada's forested ecosystems	(Hermosilla et al. 2018)
Europe	Stable Forest mask From EFDA	Conversion between Forest and other Non-Forest classes	1990,2000, 2012,2018, 2022	European Forest Disturbance Atlas (EFDA) CORINE Land Cover dataset (1990, 2000, 2006, 2012, 2018, 2022)	(Viana-Soto and Senf 2025) CORINE Land Cover, 2025
US	Forest in 2020	Conversion between Forest and other Non-Forest classes	1985-2021	Landscape Change Monitoring System (LCCMS) (Land cover layer)	USDA Forest Service (2025)
China	Forest in 2020	Conversion between Forest and other Non-Forest classes	1985-2023	China land cover dataset (CLCD)	(Yang and Huang 2021)
Tropics	Humid: Undisturbed forests/regrowth/degraded forests in 2020 Dry: tree cover >25% in 2020	Humid: Conversion between all types of forest (Undisturbed/regrowth/degraded forests) and other non-forest land cover Dry: Tree cover loss from 2000-2020, tree cover gain 2000-2012	1990-2024	Tropical Moist Forest (TMF) Tree cover, tree cover loss, and tree cover gain from Global Forest Watch (GFW)	Vancutsem et al., (2021) Hansen et al. (2013)
Australia	Forest Tree cover >20%.	Forest to other land cover (Deforestation) Other land cover to Forest (Afforestation)	1988-2023	National Forest and Sparse Woody Vegetation Data	Department of Climate Change, Energy, and the Environment and Water (2023)
Other boreal/ Other	Tree cover >25% in 2020	Tree cover loss: 2000-2020, tree cover gain 2000-2012 1990-2000: Conversion between Forest and Non-Forest classes. Cropland, oil palm, and pasture in 2020 as ancillary datasets to determine permanent tree cover loss as deforestation	2000-2020 1990,2000	Tree cover, tree cover loss, and tree cover gain from GFW Forest cover change from Global Forest Cover Change – 30 m Forest Cover Change. Forest cover change layer (1990, 2000, 2005)	Hansen et al. (2013) Townshend et al. (2017) Patapov et al. (2022) Descals et al. (2024) Parente et al. (2024)

In cases where disturbance and deforestation overlapped spatially, pixels were assigned to the disturbance category. This prioritization reflects the fact that disturbance datasets explicitly track biomass loss within forests without land-use conversion, whereas deforestation is inferred from land-cover transitions, and helps avoid double-counting of emissions. Exceptions apply in the TMF domain (Vancutsem et al., 2021) and in Australia, where datasets explicitly distinguish or allow inference between deforestation without recovery and disturbances followed by regrowth.

All disturbances, land-use transitions, and associated carbon fluxes were subsequently aggregated at the biome level using the ecoregion classification of Olson et al. (2001), which partitions global forests into tropical, temperate, and boreal biomes, with remaining areas grouped as “other”. The spatial extent of disturbance datasets and biome distribution are illustrated in Figure 3-1a.

3.2.2 Reconstructing post-disturbance biomass recovery

Post-disturbance biomass recovery was reconstructed by linking forest age (i.e., time since the most recent disturbance) derived from harmonized disturbance histories with a spatially consistent biomass baseline, following a space-for-time substitution approach (Xu et al., 2026). The procedure consisted of three main components: (i) Identification of forest age, (ii) construction of the biomass baseline, and (iii) fitting of recovery trajectories.

Forest age estimation. Forest age in 2020 was defined at 30 m resolution as the number of years elapsed since the most recent disturbance event within each pixel. When multiple disturbances occurred, only the latest event was considered. For example, if disturbances occurred in 2000 and 2005, the latter was used as the reference, yielding an age of 16 years in 2020. Recovery was assumed to begin in the year following disturbance.

Biomass baseline construction. The baseline biomass map was assembled by combining regional high-resolution datasets with a global product for areas lacking regional coverage. Regional AGB maps at 30 m resolution were used for Europe (Liu et al., 2023) and boreal forests (Varvia et al., 2024), both referenced to 2020, and for Australia (Liao et al., 2020), which represents conditions around 2010. In Australia, the regional dataset was preferred over the CCI Biomass product due to its improved representation of sparse woody vegetation. To ensure temporal consistency, forest age and recovery trajectories in Australia were aligned with the 2010 biomass reference year. For all other regions, the ESA CCI v5 Biomass product for 2020 (Santoro et al., 2024; 100 m resolution) was used and resampled to 30 m using nearest-neighbor interpolation. This approach ensures spatial consistency while retaining higher-resolution regional information where available.

Recovery curve fitting. Relationships between above-ground carbon (AGC; derived from AGB using a carbon fraction of 0.5) and forest age were established using a space-for-time approach (Heinrich et al., 2023). Biomass maps were overlaid with forest age layers to extract AGC–age pairs within each 1° grid cell. Median AGC values were calculated for each age class to reduce the influence of outliers (Xu et al., 2026). Because Landsat-based disturbance records begin around 1985–1990, observed stand ages are limited to roughly three decades. To better constrain long-term recovery, additional AGC–age information from National Forest Inventory

data (Besnard et al., 2021) was incorporated. To avoid over-weighting inventory observations and to balance contributions from different age classes, data for ages exceeding 50 years were grouped into 50-year bins, and median AGC values were used for curve fitting.

Recovery trajectories were fitted for each 1° × 1° grid cell using a Chapman–Richards function,

$$RC(t) = AGCmax \times (1-e^{-bt})^{c}+d \quad (1)$$

where t denotes time since disturbance, AGCmax represents the asymptotic biomass level, b and c control the rate and shape of recovery, and d represents residual biomass immediately after disturbance. Separate curves were fitted for fire and non-fire disturbances. The asymptotic biomass AGCmax was constrained using the 85th percentile of AGC within each grid cell, approximating mature forest conditions (Xu et al., 2026). To account for uncertainty in recovery potential, the 75th and 95th percentiles were used to define lower and upper bounds, representing structural uncertainty rather than parameter estimation uncertainty.

For afforestation and reforestation, recovery curves were fitted without distinguishing disturbance type. This choice reflects the uneven spatial distribution and limited age coverage of disturbance-specific observations, which would otherwise lead to unstable parameter estimates. A unified growth trajectory was therefore applied to ensure spatial consistency. In grid cells where recovery curves could not be reliably estimated due to insufficient observations, trajectories were inferred from neighboring grid cells within the same biome.

Validating the recovery curves. The derived recovery trajectories were evaluated using independent field-based observations compiled from the literature (Cook-Patton et al., 2020; Poorter et al., 2016; Besnard et al., 2021). The validation dataset comprised 2,288 sites and 49,644 measurements spanning multiple age classes, with contributions of approximately 2%, 76%, 0.3%, and 22% from tropical, temperate, boreal, and other biomes, respectively. As most field observations describe stand development rather than recovery following explicitly mapped disturbance events, modeled above-ground carbon (AGC) values were compared with observed AGC without separating disturbance types, using corresponding grid cells and age classes. Overall, the modeled AGC trajectories show good agreement with site-level observations across biomes (Figure 3-2), although larger deviations are evident in older stands within humid tropical regions.

To assess the representation of early-stage regrowth, biomass accumulation rates during the first 30 years following disturbance were compared with two independent global datasets of young forest regeneration (Cook-Patton et al., 2020; Robinson et al., 2025), both derived from machine-learning approaches trained on field measurements. The recovery rates estimated from our spatially explicit curves fall within the range reported by these independent products (Figure 3-3), supporting the robustness of the modeled early recovery dynamics.

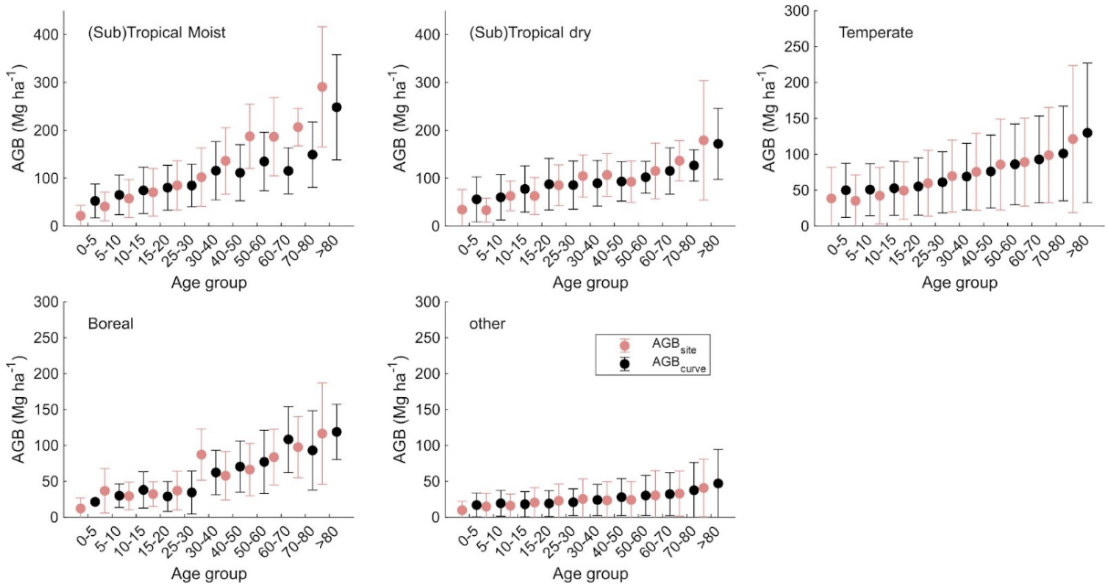

Figure 0-2. Performance of the recovery curves. AGB estimated from the recovery curves is compared with site-level AGB at corresponding ages and locations. AGB values are binned into 5-year forest-age intervals from 0–40 years and 10-year intervals for ages greater than 40 years for each forest biome. Dots represent mean AGB values from site-measured and modeled data derived from recovery curves. Error bars indicate the standard deviation.

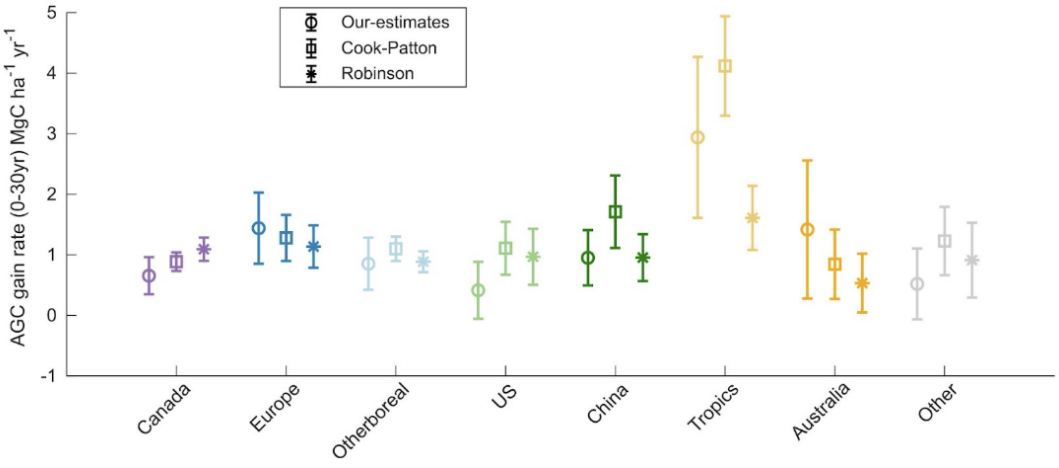

Figure 0-3. Comparison of AGC accumulation rates during the first 0-30 years after regrowth with estimates from naturally regenerating forests reported by Cook-Patton et al. (2020) and Robinson et al. (2025). Regions shown correspond to those defined in Figure 3-1b.

3.2.3 Modeling forest carbon dynamics using a spatially explicit bookkeeping model

By integrating Landsat-based forest disturbance history, forest land-use change transitions, and gridded recovery curves, we estimated AGC changes across global forests from 1990 to 2020 using a data-driven, spatially explicit bookkeeping model.

Carbon gains and losses from forest disturbances. For each disturbance event followed by forest recovery, post-disturbance biomass gains were determined by reading the recovery curves at the corresponding grid and the elapsed time between successive disturbance events. The recovery curves for fire and other non-fire disturbances were applied for each type of disturbance event.

For the other non-fire disturbances, AGC loss was calculated as the difference between pre-disturbance AGC and the remaining living biomass after disturbance [AGCloss_NonFire=AGCpre-AGCremain]. For pixels with prior disturbances, pre-disturbance AGC was inferred from the recovery curve using the time since the previous disturbance. For pixels experiencing their first recorded disturbance, pre-disturbance AGC was approximated by the mean AGC of the N surrounding undisturbed forest pixels (N = 10). The remaining biomass was computed as pre-disturbance AGC multiplied by the remaining biomass fraction, defined as [fractionremain=d/AGCmax], where AGCmax and d are the maximum biomass and intercept of the corresponding recovery curve.

Following each fire disturbance, excluding the remaining biomass surviving from the fire, not all the forest biomass supposed to be combusted is instantaneously combusted and emitted to the atmosphere at the time of burning. A fraction of the uncombusted biomass is converted into necromass (i.e., fire-formed coarse woody debris, CWD), which releases carbon gradually to the atmosphere through decomposition. We therefore applied a global combustion completeness from Van Wees et al. (2022) at 500m resolution to distinguish between instantaneous burning emissions and carbon transferred to the CWD. The legacy emissions from CWD decomposition were represented using an exponential decay function (Harmon et al., 2021). The decay rates were derived from a global synthesis (Zanne et al., 2021) and spatially allocated using nearest-neighbor interpolation. During CWD decomposition, only partial C is released to the atmosphere. To account for this, we applied a ratio of carbon use efficiency, which partitions C transferring from litter into the soil in the calculation, following the parameterization from the Century model.

Carbon changes from forest land-use change. Carbon gains for afforested or reforested pixels were estimated using growth curves (derived from combined fire and non-fire disturbances) at the corresponding grid cell and the duration of regrowth before any subsequent disturbance or land-use change. Conversely, carbon losses from deforested pixels were quantified based on the pre-deforestation AGC. This initial AGC was determined by the previous recovery or growth trajectory if the pixel had a history of disturbance or conversion. In the absence of prior changes, we used the mean AGC of surrounding undisturbed forest pixels.

Carbon gains from forests without mapped disturbances. To assess carbon gains in remaining undisturbed forests, we delineated their extent by excluding pixels with recorded disturbances or land-use changes from the 2020 forest baseline. This baseline was compiled from regional land cover products and global tree cover datasets (Table 3-2). For each undisturbed pixel, we extracted AGC values from the 2020 baseline biomass map and estimated

forest age using a backcasting approach. This involved inverting the biomass recovery curves fitted for the corresponding 1° × 1° grid cell. We then estimated AGC accumulation from 1985 to 2020 by calculating the difference in biomass between the inferred forest ages in 2020 and 1985 [Gainundist=AGCage=2020−AGCage=1985].

This approach assumes that forests free of detected disturbances since 1985 may still be recovering from pre-1985 events and follow the same recovery trajectories of recently disturbed forests. However, uncertainties arise regarding whether these older undisturbed forests strictly follow these recent disturbance trajectories and whether the backcasting approach accurately predicts forest age. We therefore conducted two sensitivity tests. First, we evaluated carbon gains in tropical forests using inventory-based forest regeneration curves (Poorter et al., 2016; Cook-Patton et al., 2020). Second, we substituted our backcasted ages with an alternative global forest age map at 100 m resolution (Besnard et al., 2025) while using our satellite-derived recovery curves. Estimates based on inventory curves and satellite-derived curves yielded comparable carbon gains for undisturbed tropical forests (20 vs. 25 Pg C). Similarly, the backcasting approach and the global forest age map produced consistent total carbon gains for undisturbed forests (35 vs. 40 Pg C) over the study period.

3.3 Fire dominates disturbance-driven forest carbon losses

We first quantified gross above-ground carbon (AGC) losses from forest disturbances within forests remaining forests, excluding emissions associated with deforestation and afforestation. Fire-related losses include both immediate emissions from combustion and delayed emissions from the decomposition of fire-generated dead biomass (e.g., coarse woody debris; Methods).

During 1990–2020, fires were the dominant source of disturbance-related forest carbon losses globally, accounting for 57% (15.2 PgC) of total losses, whereas non-fire disturbances (e.g., logging, insects) contributed 11.3 PgC (Figure 3-4a). This dominance of fire is particularly evident in boreal and tropical forests, where it explains 55% (1.0 PgC) and 66% (~13.5 PgC) of total disturbance-driven losses, respectively. In contrast, temperate forests exhibit a markedly different disturbance regime, with non-fire processes accounting for 91% of total carbon losses (Figure 3-4b).

At the regional scale, while African dry tropical forests dominate in terms of cumulative fire-related losses, the highest loss intensities (i.e., carbon loss per unit burned area) occur in carbon-dense humid forests, such as those in the Amazon, Borneo, and northeastern Australia (Figure 3-3c). In contrast, hotspots of non-fire disturbance-related losses are located in the central Congo Basin, southern Canada, and central Europe (Figure 3-4d), reflecting regions with frequent harvesting and other non-fire disturbance processes, including shifting cultivation in parts of the Congo Basin (Molinario et al., 2017).

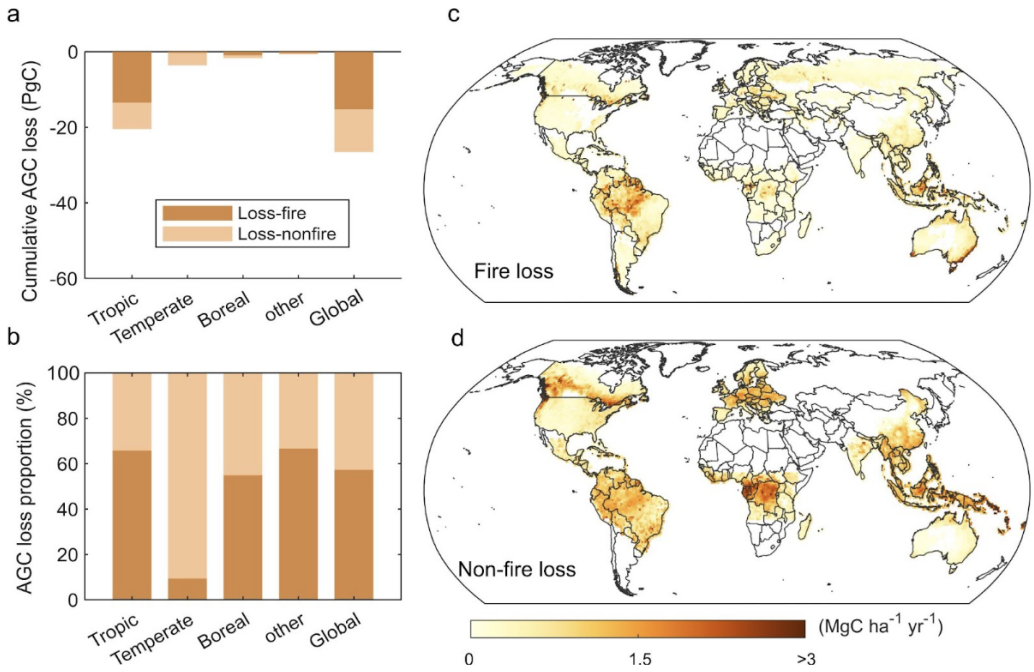

Figure 0-4. Gross carbon losses from non-deforestation forest disturbances (1990–2020). (a, b) Cumulative above-ground carbon (AGC) losses and relative contributions of fire and non-fire disturbances across biomes (see also Figure S4). Values are aggregated over 1990–2020 (PgC), with fractions indicating the proportional contribution of each disturbance type. (c, d) Spatial distribution of mean annual gross carbon losses (Mg C ha^{-1} yr^{-1}) associated with fire (c) and non-fire (d) disturbances over the 30-year period. In regions lacking regional disturbance datasets (e.g., boreal Asia), non-fire disturbances are not quantified; in these areas, fire-related losses are derived solely from a global burned-area product (Methods).

3.4 Trends in gross fire carbon losses are primarily driven by carbon loss intensity

We analyzed temporal changes in disturbance-related carbon losses, disturbed area, and carbon loss per unit area over the period 2000–2020. This time window was selected due to limitations in Landsat-based disturbance observations prior to 2000, including gaps in burned-area records during the 1990s in tropical and Russian boreal regions.

In boreal forests, annual fire-related carbon losses show a significant increase over 2000–2020. This trend is primarily driven by rising carbon loss per unit burned area (hereafter referred to as loss intensity), while total burned area does not exhibit a significant trend at the biome scale (Figure 3-5a). Loss intensity increased by approximately 5.2 Mg C ha^{-1} over this period, indicating that fires are increasingly affecting carbon-dense forests and/or becoming more severe. This pattern is consistent with previous studies reporting increasing fire emissions despite stable or declining burned areas (Zheng et al., 2023; Jones et al., 2024). In contrast, tropical forests show a decline in fire-related gross AGC losses over the same period (Figure 3-5c). This decrease is associated with a reduction in loss intensity (−2.1 Mg C ha^{-1} over 2000–2020), while burned area remains statistically unchanged. The simultaneous decline in both total fire losses and loss intensity is consistent with increasing fire recurrence, particularly in dry tropical regions (Xu et al., 2026; Armenteras et al., 2021), which reduces available fuel loads and limits biomass loss in subsequent fires (Saito et al., 2014). Fire-related losses in temperate forests remain comparatively low and show no significant temporal trend.

For non-fire disturbances, gross carbon losses exhibit an overall declining trend across biomes since 2000, despite episodic peaks in specific years (e.g., 2015 in tropical regions and 2020 in temperate regions; Figure 3-5). Unlike fire-driven losses, these trends are primarily explained by reductions in disturbed area, particularly in tropical and temperate forests, while loss intensity shows an increasing tendency. Boreal non-fire trends are not analyzed in detail due to limited data coverage, especially the lack of consistent disturbance records in Russia. The observed increase in loss intensity suggests that non-fire disturbances are increasingly affecting higher-biomass forests, implying a shift toward more carbon-intensive disturbances that is not captured by changes in area alone. This pattern is consistent with the strong influence of human activities and likely reflects changes in disturbance location, intensity, and management practices rather than a reduction in disturbance pressure.

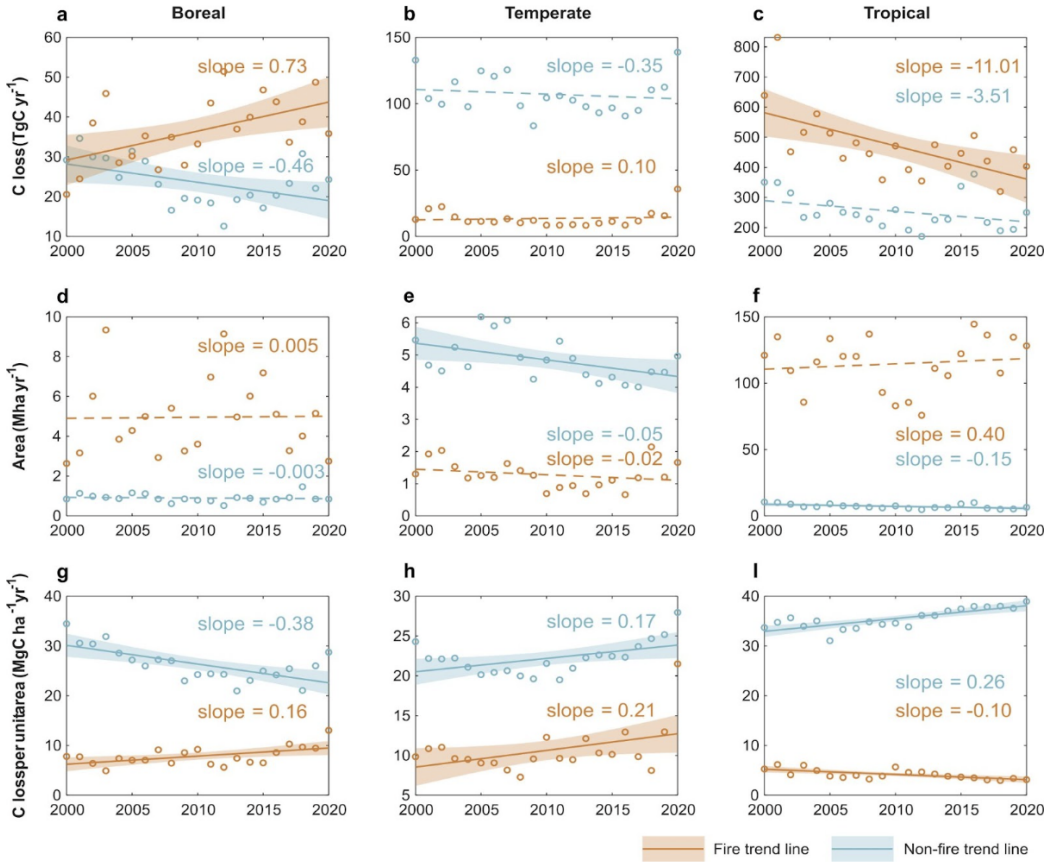

Figure 0-5. Temporal trends in disturbance-related carbon losses, disturbed area, and loss intensity across biomes (2000–2020). (a–c) Annual gross above-ground carbon (AGC) losses from fire (orange) and non-fire (blue) disturbances. (d–f) Disturbed area associated with fire and non-fire events. (g–i) Carbon loss per unit burned/disturbed area (loss intensity). Panels are organized by biome: boreal (a, d, g), temperate (b, e, h), and tropical (c, f, i). Solid lines denote statistically significant linear trends ($P < 0.05$), with slopes indicated, while dashed lines represent non-significant trends.

3.5 Post-fire recovery offsets most fire-related carbon losses

By combining disturbance records with our gridded post-disturbance recovery curves (Methods), we estimated biomass recovery following disturbances and the resulting net carbon impact from fire and non-fire disturbances. Across global forests, biomass regrowth following fires since 1990 contributed 14.2 PgC of cumulative carbon gains, offsetting approximately 93% of cumulative

fire-related carbon emissions by 2020 (Figure 3-6). The higher recovery rates are observed in regions such as continental Europe, southeastern Canada, the northwestern Amazon, and northern Australia (Figure 3-6c), indicating strong spatial variability in recovery rate.

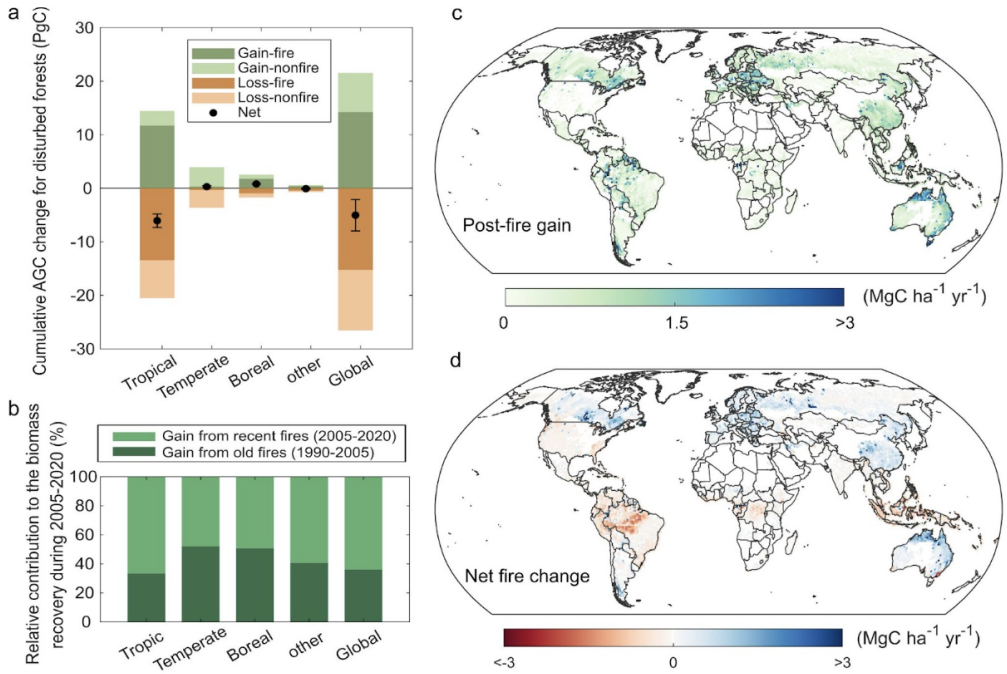

Figure 0-6. Carbon losses from fire and post-fire biomass recovery in forests affected by fires during 1990–2020. (a) Cumulative above-ground carbon (AGC) emissions from fire and corresponding post-fire biomass recovery gains over 1990–2020. Black points with error bars indicate the resulting net AGC change and associated standard errors. (b) Contribution of legacy effects to post-fire recovery by biome, showing the relative share (%) of biomass gains during 2005–2020 attributable to fires occurring in 1990–2005 ("older fires") and 2005–2020 ("recent fires"). (c) Spatial distribution of post-fire biomass recovery, expressed as mean annual carbon gain per unit area (Mg C ha^{-1} yr^{-1}) averaged over 1990–2020. (d) Spatial distribution of net fire-related forest biomass carbon change (Mg C ha^{-1} yr^{-1}) over 1990–2020, calculated as the balance between fire-induced carbon losses and post-fire recovery gains.

Post-fire recovery reflects not only recent disturbances but also the legacy of past fire events. Forests burned during 1990–2005 (hereafter "older fires") contribute 36% (3.2 PgC) of the recovery observed during 2005–2020, with the remaining share attributed to more recent fires (2005–2020) (Figure 3-6b). The relative contribution of these cohorts varies across biomes. In boreal forests, slower regrowth leads to a larger contribution from older fires (51%), whereas in tropical forests, faster recovery results in a greater contribution from recent fires (67%) to total post-fire carbon gains (Figure 3-6b).

When post-fire recovery is taken into account, the gross fire-related carbon loss of 15.2 PgC over 1990–2020 is reduced to a net loss of 1.0 PgC. Spatially, fire-affected boreal forests since 1990 function as a modest net carbon sink, despite increasing fire emissions in recent years, because ongoing recovery from earlier disturbances continues to offset recent losses. In contrast, tropical forests remain a net carbon source, as cumulative fire-induced losses still exceed recovery gains, even though fire emissions have declined (Figures 3-4 and 3-5d). These results highlight that the net carbon effect of fire is governed by the balance between immediate disturbance-driven losses and recovery processes that integrate both recent and legacy disturbances.

3.6 Fire contributes substantially to the full forest carbon budget

By integrating carbon fluxes from fire and non-fire disturbances, land-use change (deforestation and afforestation), and growth in forests without recorded disturbances since 1990 (Methods), we constructed a full above-ground carbon (AGC) budget for global forests over 1990–2020 (Figure 3-7). The estimated cumulative carbon loss from deforestation (18 PgC) is consistent with bookkeeping model estimates (19 PgC) (Figures 3-8), with the largest losses occurring in tropical regions .

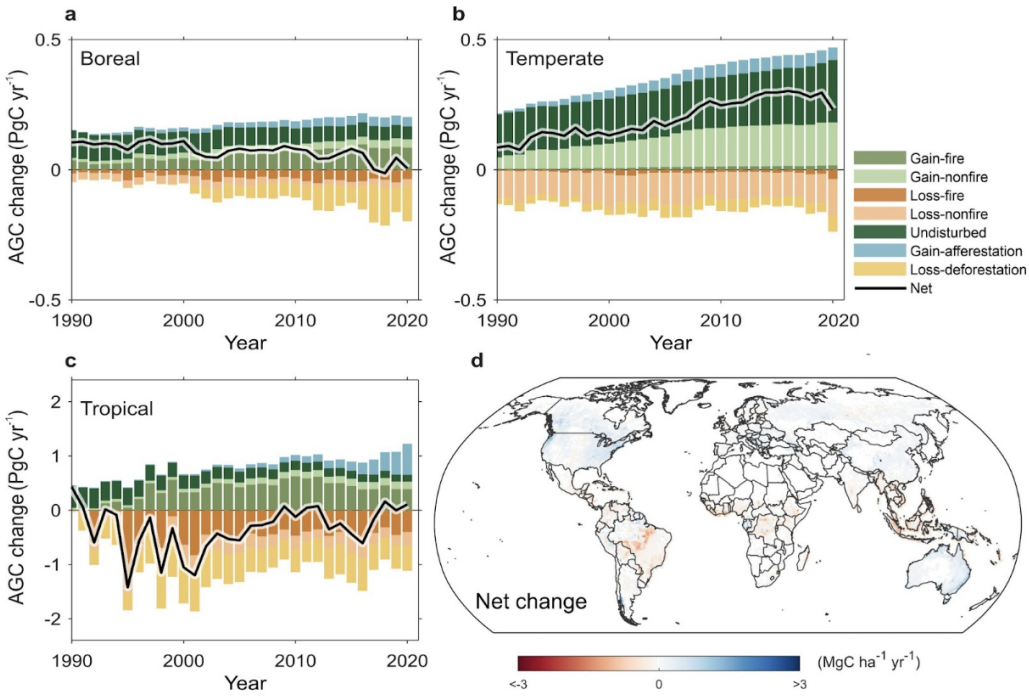

Figure 0-7. Spatial and temporal dynamics of forest carbon balance (1990–2020). (a–c) Temporal evolution of above-ground carbon (AGC) fluxes by biome. Bars represent annual carbon losses and gains from fire and non-fire disturbances, deforestation, afforestation, and growth in undisturbed forests. Black lines indicate the net AGC balance, calculated as the sum of all flux components. Panels correspond to boreal (a), temperate (b), and tropical (c) forests. (d) Spatial distribution of mean annual net AGC change (Mg C ha^{-1} yr^{-1}) over 1990–2020, integrating carbon losses from disturbances and deforestation with gains from post-disturbance recovery, growth in undisturbed forests, and afforestation.

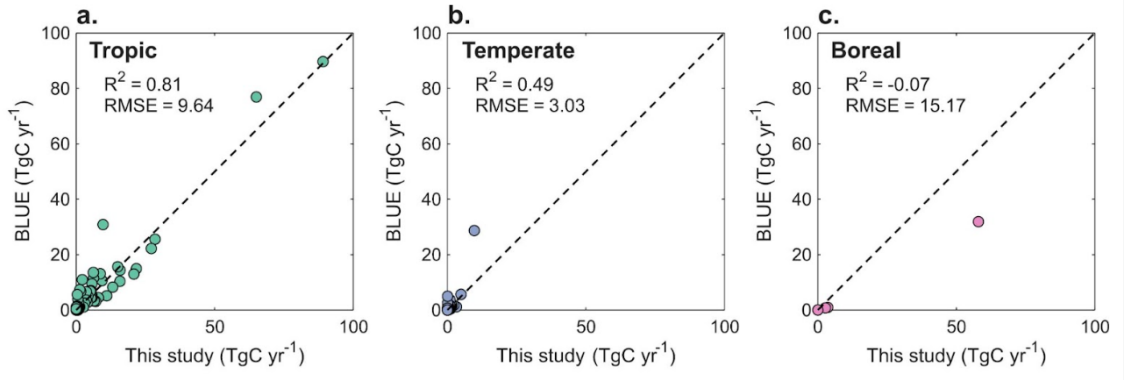

Figure 0-8. Country-level comparison of deforestation-related AGC losses between this study and the BLUE bookkeeping model for 2000–2020 across (a) tropical, (b) temperate, and (c) boreal regions. The dashed line represents the 1:1 line.

At the global scale, forests exhibited a near-neutral above-ground carbon (AGC) balance over the study period. , with gross losses of 44.5 PgC nearly offset by gross gains of 44.2 PgC, resulting in a small net loss of 0.4 PgC. This finding is consistent with recent large-scale assessments based on inventory and remote sensing data (Bar-On et al., 2025; Randerson et al., 2025).

Within this full budget, fire represents a major component of forest carbon fluxes, contributing 34% of cumulative losses and 32% of cumulative gains globally. However, its net impact varies markedly across biomes. Boreal and temperate forests function as net carbon sinks, with cumulative gains of 3.4 PgC and 6.6 PgC, respectively. In boreal regions, fire contributes positively to the net carbon balance (25% of net gains), driven by sustained post-fire recovery. In contrast, fire has a negligible net effect in temperate forests (−1%), where non-fire disturbances dominate the carbon fluxes.

Tropical forests, by contrast, act as a net carbon source (−11 PgC) over 1990–2020. Although fire contributes substantially to both gross losses (38%) and gains (47%), rapid recovery limits its net contribution to 17% of total carbon losses. Instead, deforestation (−14.8 PgC) remains the dominant driver of carbon change in the tropics, followed by non-fire disturbances (−7.0 PgC). For consistency with regional studies, non-fire degradation processes in the tropics are included within the non-fire disturbance category.

More broadly, the substantial contribution of fire to both gross losses and recovery gains indicates that shifts in fire behaviour could strongly affect the future forest carbon budget. This is particularly relevant given recent evidence that forest fire carbon emissions have increased markedly since 2001, with the strongest increases occurring in extratropical forests, especially boreal North America and Eurasia (Jones et al., 2024).

3.7 Conclusion

By harmonizing the global disturbance history from multiple regional datasets, we estimate forest carbon losses and recovery associated with fire and non-fire disturbances across global forests from 1990 to 2020, using a spatially explicit bookkeeping model integrated with a global set of gridded biomass recovery curves. We show that fire dominates disturbance-driven forest AGC losses globally, accounting for 55% and 66% of gross losses in boreal and tropical forests, while non-fire disturbances (91%) dominate losses in temperate forests. Since 2000, increasing fire-related carbon losses in boreal forests are driven primarily by rising carbon loss per unit area rather than by

increasing burned area. In contrast, declining carbon losses in tropical forests are associated with reduced biomass loss density, consistent with increasing fire recurrence and progressively limited available fuel loads. Biomass recovery following fires sequestered 14.2 PgC since 1990, which has offset 93% of fire-related carbon losses (15.2 PgC). When placed in the context of the full global forest carbon budget, including forest land-use change and growth of forests that did not experience disturbances since 1990, we show that fire-related losses and recovery account for one-third of total forest carbon changes. However, our analysis focuses on AGC, it does not include fire emissions from soil combustion or below-ground biomass (BGB), and therefore may underestimate the full carbon impact of fire. Our findings reveal the under-represented role of fire in current modelling and inventory frameworks, and highlight the importance of preventing high-severity fires in carbon-rich forests as well as enhancing post-fire recovery in regions with high capacity.

3.8 References

Anderegg, William R. L., Anna T. Trugman, Grayson Badgley, et al. 2020. “Climate-Driven Risks to the Climate Mitigation Potential of Forests.” Science (New York, N.Y.) 368 (6497). https://doi.org/10.1126/science.aaz7005.

Armenteras, Dolors, Liliana M. Dávalos, Joan S. Barreto, et al. 2021. “Fire-Induced Loss of the World’s Most Biodiverse Forests in Latin America.” Science Advances 7 (33). https://doi.org/10.1126/sciadv.abd3357.

Bar-On, Yinon M., Xiaojun Li, Michael O’Sullivan, et al. 2025. “Recent Gains in Global Terrestrial Carbon Stocks Are Mostly Stored in Nonliving Pools.” Science (New York, N.Y.) 387 (6740): 1291–1295.

Bellen, Simon van, Michelle Garneau, and Yves Bergeron. 2010. “Impact of Climate Change on Forest Fire Severity and Consequences for Carbon Stocks in Boreal Forest Stands of Quebec, Canada: A Synthesis.” Fire Ecology 6 (3): 16–44.

Besnard, Simon, Viola H. A. Heinrich, Nuno Carvalhais, et al. 2025. “Global Covariation of Forest Age Transitions with the Net Carbon Balance.” Nature Ecology & Evolution 9 (10): 1848–1860.

Brando, P. M., B. Soares-Filho, L. Rodrigues, et al. 2020. “The Gathering Firestorm in Southern Amazonia.” Science Advances 6 (2): eaay1632.

Cook-Patton, S. C. et al. Mapping carbon accumulation potential from global natural forest regrowth. Nature 585, 545-550, doi:10.1038/s41586-020-2686-x (2020).

Department of Climate Change, Energy, the Environment and Water (2023). National forest and sparse woody vegetation data. Version 8.0. Commonwealth of Australia, Canberra.

Descals, Adrià, David L. A. Gaveau, Serge Wich, Zoltan Szantoi, and Erik Meijaard. 2024. “Global Mapping of Oil Palm Planting Year from 1990 to 2021.” Earth System Science Data 16 (11): 5111–5129.

Dye, Alex W., Rachel M. Houtman, Peng Gao, et al. 2024. “Carbon, Climate, and Natural Disturbance: A Review of Mechanisms, Challenges, and Tools for Understanding Forest Carbon Stability in an Uncertain Future.” Carbon Balance and Management 19 (1): 35.

European Environment Agency (EEA). 2025. CORINE Land Cover (CLC). Copernicus Land Monitoring Service. https://land.copernicus.eu/

FAO. 2022. Global Forest Resources Assessment 2020: Remote Sensing Survey. Rome: Food and Agriculture Organization of the United Nations.

Varvia, Petri, et al. "Estimation of boreal forest biomass from ICESat-2 data using hierarchical hybrid inference." Remote Sensing of Environment 311 (2024): 114249.

Friedlingstein, Pierre, Michael O'Sullivan, Matthew W. Jones, et al. 2025. "Global Carbon Budget 2024." Earth System Science Data 17 (3): 965–1039.

Gibbs, David A., Melissa Rose, Giacomo Grassi, et al. 2025. "Revised and Updated Geospatial Monitoring of 21st Century Forest Carbon Fluxes." Earth System Science Data 17 (3): 1217–1243.

Grassi, Giacomo, Clemens Schwingshackl, Thomas Gasser, et al. 2023. "Harmonising the Land-Use Flux Estimates of Global Models and National Inventories for 2000–2020." Earth System Science Data 15 (3): 1093–1114.

Hansen, M. C. et al. High-resolution global maps of 21st-century forest cover change. Science 342, 850–853 (2013).

Harris, Nancy L., David A. Gibbs, Alessandro Baccini, et al. 2021. "Global Maps of Twenty-First Century Forest Carbon Fluxes." Nature Climate Change 11 (3): 234–240.

Harmon, M. E. et al. Release of coarse woody detritus-related carbon: a synthesis across forest biomes. Carbon Balance and Management 15, 1, doi:10.1186/s13021-019-0136-6 (2020).

Heinrich, Viola H. A., Christelle Vancutsem, Ricardo Dalagnol, et al. 2023. "The Carbon Sink of Secondary and Degraded Humid Tropical Forests." Nature 615 (7952): 436–442.

Hermosilla, Txomin, Michael A. Wulder, Joanne C. White, and Nicholas C. Coops. 2019. "Prevalence of Multiple Forest Disturbances and Impact on Vegetation Regrowth from Interannual Landsat Time Series (1985–2015)." Remote Sensing of Environment 233 (111403): 111403.

Hermosilla, Txomin, Michael A. Wulder, Joanne C. White, Nicholas C. Coops, and Geordie W. Hobart. 2018. "Disturbance-Informed Annual Land Cover Classification Maps of Canada's Forested Ecosystems for a 29-Year Landsat Time Series." Canadian Journal of Remote Sensing/Journal Canadien de Teledetection 44 (1): 67–87.

Holcomb, Amelia, Simon V. Mathis, David A. Coomes, and Srinivasan Keshav. 2023. "Computational Tools for Assessing Forest Recovery with GEDI Shots and Forest Change Maps." Science of Remote Sensing 8 (100106): 100106.

Izbicki, Brian, Xanthe J. Walker, Jennifer L. Baltzer, et al. 2023. "Drivers of Legacy Soil Organic Matter Decomposition after Fire in Boreal Forests." Ecosphere (Washington, D.C) 14 (11). https://doi.org/10.1002/ecs2.4672.

IPCC (2006) – 2006 IPCC Guidelines for National Greenhouse Gas Inventories Volume 4: Agriculture, Forestry and Other Land Use (AFOLU)

Jones, Matthew W., Sander Veraverbeke, Niels Andela, et al. 2024. "Global Rise in Forest Fire Emissions Linked to Climate Change in the Extratropics." Science (New York, N.Y.) 386 (6719): eadl5889.

Lapola, David M., Patricia Pinho, Jos Barlow, et al. 2023. "The Drivers and Impacts of Amazon Forest Degradation." Science (New York, N.Y.) 379 (6630): eabp8622.

Liu, Siyu, Martin Brandt, Thomas Nord-Larsen, et al. 2023. "The Overlooked Contribution of Trees Outside Forests to Tree Cover and Woody Biomass across Europe." Science Advances, ahead of print, September. https://doi.org/10.1126/sciadv.adh4097.

Liu, Z., Wang, W.J., Ballantyne, A. et al. Forest disturbance decreased in China from 1986 to 2020 despite regional variations. Commun Earth Environ 4, 15 (2023). https://doi-org.ezproxy.universite-paris-saclay.fr/10.1038/s43247-023-00676-x

Liao Z, Van Dijk AI, He B, Larraondo PR, Scarth PF. Woody vegetation cover, height and biomass at 25-m resolution across Australia derived from multiple site, airborne and satellite observations. International Journal of Applied Earth Observation and Geoinformation. 2020 Dec 1;93:102209.

Long, Tengfei, Zhaoming Zhang, Guojin He, et al. 2019. "30 M Resolution Global Annual Burned Area Mapping Based on Landsat Images and Google Earth Engine." Remote Sensing 11 (5): 489

Molinario, Giuseppe, Matthew Hansen, and Peter V. Potapov. 2017. "Forest Cover Dynamics of Shifting Cultivation in the Democratic Republic of the Congo 2000–2010 (2015 Environ. Res. Lett. 10 094009)." Environmental Research Letters 12 (8): 089501.

Mack, Michelle C., Xanthe J. Walker, Jill F. Johnstone, et al. 2021. "Carbon Loss from Boreal Forest Wildfires Offset by Increased Dominance of Deciduous Trees." Science (New York, N.Y.) 372 (6539): 280–283.

Miguel, Sergio de-, Abdi Birhanu, Imma Oliveras Menor, Davide Ascoli, Gian Luca Spadoni, and Maitane Erdozain. 2025. "Carbon Emissions from Forest Disturbances under Global Change." Current Forestry Reports 11 (1). https://doi.org/10.1007/s40725-025-00257-5.

O'Sullivan, Michael, Stephen Sitch, Pierre Friedlingstein, et al. 2024. "The Key Role of Forest Disturbance in Reconciling Estimates of the Northern Carbon Sink." Communications Earth & Environment 5 (1). https://doi.org/10.1038/s43247-024-01827-4.

Olson, D. M., Dinerstein, E., Wikramanayake, E. D., Burgess, N. D., Powell, G. V. N., Underwood, E. C., D'Amico, J. A., Itoua, I., Strand, H. E., Morrison, J. C., Loucks, C. J., Allnutt, T. F., Ricketts, T. H., Kura, Y., Lamoreux, J. F., Wettengel, W. W., Hedao, P., & Kassem, K. R. (2001). Terrestrial Ecoregions of the World: A New Map of Life on Earth. BioScience, 51(11), 933–938. https://doi.org/10.1641/0006-3568(2001)051[0933:TEOTWA]2.0.CO;2

Palviainen, M., A. Laurén, J. Pumpanen, et al. 2020. "Decadal-scale Recovery of Carbon Stocks after Wildfires throughout the Boreal Forests." Global Biogeochemical Cycles 34 (8). https://doi.org/10.1029/2020gb006612.

Poorter, Lourens, Frans Bongers, T. Mitchell Aide, et al. 2016. "Biomass Resilience of Neotropical Secondary Forests." Nature 530 (7589): 211–214.

Poorter, Lourens, Dylan Craven, Catarina C. Jakovac, et al. 2021. "Multidimensional Tropical Forest Recovery." Science (New York, N.Y.) 374 (6573): 1370–1376.

Parente, Leandro, Lindsey Sloat, Vinicius Mesquita, et al. 2024. "Annual 30-M Maps of Global Grassland Class and Extent (2000-2022) Based on Spatiotemporal Machine Learning." Scientific Data 11 (1): 1303.

Potapov, Peter, Svetlana Turubanova, Matthew C. Hansen, et al. 2022. "Global Maps of Cropland Extent and Change Show Accelerated Cropland Expansion in the Twenty-First Century." Nature Food 3 (1): 19–28.

Qiu, Shi, Zhe Zhu, Xiucheng Yang, et al. 2025. “A Shift from Human-Directed to Undirected Wild Land Disturbances in the USA.” Nature Geoscience 18 (10): 989–996.

Randerson, James T., Yue Li, Weiwei Fu, et al. 2025. “The Weak Land Carbon Sink Hypothesis.” Science Advances 11 (37): eadr5489.

Robinson, Nathaniel, C. Ronnie Drever, David A. Gibbs, et al. 2025. “Protect Young Secondary Forests for Optimum Carbon Removal.” Nature Climate Change 15 (7): 793–800.

Saito, Makoto, Sebastiaan Luyssaert, Ben Poulter, et al. 2014. “Fire Regimes and Variability in Aboveground Woody Biomass in Miombo Woodland.” Journal of Geophysical Research. Biogeosciences 119 (5): 1014–1029.

Santoro, M. et al. Design and performance of the Climate Change Initiative Biomass global retrieval algorithm. Science of Remote Sensing 10, 100169, doi:https://doi.org/10.1016/j.srs.2024.100169 (2024).

Seidl, Rupert, Dominik Thom, Markus Kautz, et al. 2017. “Forest Disturbances under Climate Change.” Nature Climate Change 7 (6): 395–402.

Townshend, J. (2016). Global Forest Cover Change (GFCC) Forest Cover Change Multi-Year Global 30 m V001 [Data set]. NASA Land Processes Distributed Active Archive Center. https://doi.org/10.5067/MEASURES/GFCC/GFCC30FCC.001 Date Accessed: 2026-02-12

United States Geological Survey, US Forest Service, and Kurtis Nelson. 2021. “Monitoring Trends in Burn Severity (ver. 12.0, April 2025).” U.S. Geological Survey. https://doi.org/10.5066/P9IED7RZ.

Vancutsem, C., F. Achard, J-F Pekel, et al. 2021. “Long-Term (1990-2019) Monitoring of Forest Cover Changes in the Humid Tropics.” Science Advances 7 (10). https://doi.org/10.1126/sciadv.abe1603.

van Wees, D. et al. Global biomass burning fuel consumption and emissions at 500 m spatial resolution based on the Global Fire Emissions Database (GFED). Geosci. Model Dev. 15, 8411-8437, doi:10.5194/gmd-15-8411-2022 (2022).

Viana-Soto, Alba, and Cornelius Senf. 2025. “The European Forest Disturbance Atlas: A Forest Disturbance Monitoring System Using the Landsat Archive.” Earth System Science Data 17 (6): 2373–2404.

Werf, Guido R. van der, James T. Randerson, Dave van Wees, et al. 2025. “Landscape Fire Emissions from the 5th Version of the Global Fire Emissions Database (GFED5).” Scientific Data 12 (1): 1870.

Xu, Yidi, Philippe Ciais, Maurizio Santoro, et al. 2026. “Small Persistent Humid Forest Clearings Drive Tropical Forest Biomass Losses.” Nature 649 (8096): 375–380.

Yang, Jie, and Xin Huang. 2021. “The 30 M Annual Land Cover Dataset and Its Dynamics in China from 1990 to 2019.” Earth System Science Data 13 (8): 3907–3925.

Zheng, Bo, Philippe Ciais, Frederic Chevallier, et al. 2023. “Record-High CO Emissions from Boreal Fires in 2021.” Science (New York, N.Y.) 379 (6635): 912–917.

Zanne, A. E. et al. Termite sensitivity to temperature affects global wood decay rates. Science 377, 1440-1444, doi:doi:10.1126/science.abo3856 (2022).